Modelling and assimilation of lidar signals over Greater Paris during the MEGAPOLI summer campaign

Y. Wang[1,2], K.N. Sartelet[1], M. Bocquet[1,3], and P. Chazette[2]

[1]CEREA, joint laboratory École des Ponts ParisTech - EDF R&D, Université Paris-Est, 77455 Champs-sur-Marne, France
[2]LSCE, joint laboratory CEA-CNRS, UMR8212, 91191 Gif-sur-Yvette, France
[3]INRIA, Paris-Rocquencourt Research Center, Le Chesnay, France

Correspondence to: Y. Wang
(wangy@cerea.enpc.fr)

Abstract. In this study, we investigate the ability of the chemistry transport model (CTM) PO-LAIR3D of the air quality modelling platform POLYPHEMUS to simulate lidar backscattered profiles from model aerosol concentration outputs. This investigation is an important preprocessing stage of data assimilation (validation of the observation operator). To do so, simulated lidar signals are

5 compared to hourly lidar observations performed during the MEGAPOLI (Megacities: Emissions, urban, regional and Global Atmospheric POLlution and climate effects, and Integrated tools for assessment and mitigation) summer experiment in July 2009, where a ground-based mobile lidar was deployed around Paris on-board a van. The comparison is performed for six different measurement days, 01, 04, 16, 21, 26 and 29 July 2009, corresponding to different levels of pollution and dif-

10 ferent atmospheric conditions. Overall, POLYPHEMUS reproduces well the vertical distribution of lidar signals and their temporal variability, especially for 01, 16, 26 and 29 July 2009. Discrepancies on 04 and 21 July 2009 are due to high-altitude aerosol layers, which are not well modelled. In the second part of this study, two new algorithms for assimilating lidar observations based on the optimal interpolation method are presented. One algorithm analyses PM_{10} (particulate matter with

15 diameter less than 10 μm) concentrations. Another analyses $PM_{2.5}$ (particulate matter with diameter less than 2.5 μm) and $PM_{2.5-10}$ (particulate matter with a diameter higher than 2.5 μm and lower than 10 μm) concentrations separately. The aerosol simulations without and with lidar data assimilation are evaluated using the Airparif (a regional operational network in charge of air quality survey around the Paris area) data base to demonstrate the feasibility and the usefulness of assimilating lidar

20 profiles for aerosol forecasts. The evaluation shows that data assimilation (DA) is more efficient at correcting PM_{10} than $PM_{2.5}$, probably because $PM_{2.5}$ is better modelled than PM_{10}. Furthermore,

the algorithm which analyses both $PM_{2.5}$ and $PM_{2.5-10}$ provides the best scores for PM_{10}. The averaged RMSE of PM_{10} is 11.63 $\mu g\,m^{-3}$ with DA ($PM_{2.5}$ and $PM_{2.5-10}$), against 13.69 $\mu g\,m^{-3}$ with DA (PM_{10}) and 17.74 $\mu g\,m^{-3}$ without DA on 01 July 2009. The averaged RMSE of PM_{10}

25   is 4.73 $\mu g\,m^{-3}$ with DA ($PM_{2.5}$ and $PM_{2.5-10}$), against 6.08 $\mu g\,m^{-3}$ with DA (PM_{10}) and 6.67 $\mu g\,m^{-3}$ without DA on 26 July 2009.

1   Introduction

Aerosols are key air quality species to monitor and model as they impact vegetation and as they impact human health by penetrating the respiratory system and leading to respiratory and cardiovas-

30   cular diseases (Kelly et al., 2011; Lauwerys et al., 2007; Dockery and Pope, 1996). They also impact visibility (Wang et al., 2009), and they represent an uncertain component of climate changes due to their effects on the Earth's radiative budget (Intergovernment Panel on Climate Control (IPCC), 2007). For air quality, in order to simulate and predict particle concentrations, modellers have developed various chemistry transport models (CTM), e.g. EMEP (European Monitoring and Evaluation

35   Programme) (Simpson et al., 2003), LOTOS (Long Term Ozone Simulation) - EUROS (European Operational Smog) (Schaap et al., 2004), CHIMERE (Hodzic et al., 2006), DEHM (Danish Eulerean Hemispheric Model) (Brandt et al., 2007) and POLYPHEMUS (Sartelet et al., 2007). However, the aerosol vertical distribution is poorly quantified, because of numerous uncertainties on their sources (direct emissions) and on processes affecting their formation, e.g. nucleation, condensation, evap-

40   oration, and coagulation, as well as on meteorological conditions. Since aerosol lifetime ranges from 1 to 10 days (Seinfeld and Pandis, 1998), improvements in the representation of their vertical distribution may lead to improved surface concentrations (lower error and higher correlation against observations) (Wang et al., 2013).

     Various measurement types have been used to evaluate these models. The most frequently used

45   data are *in situ* surface measurements, e.g. AirBase (http://www.eea.europa.eu/) and EMEP over Europe, BDQA (Base de Données de la Qualité de l'Air) (Sartelet et al., 2007; Konovalov et al., 2009). However, they do not provide direct information on vertical profiles.

     Satellite passive remote sensors (e.g. the Moderate Resolution Imaging Spectroradiometers (MODIS)) and sun-photometer surface stations (e.g. the AErosol RObotic NETwork (AERONET)) have greatly

50   enhanced our ability to evaluate such models. Comparisons between observed and simulated Aerosol Optical Depth (AOD) have been performed for global models and regional models (Kinne et al., 2006; Tombette et al., 2008; Péré et al., 2010). However, instruments, such as sun photometers can only retrieve column-integrated aerosol properties and can only work during daytime.

     Since accurate vertical profiles of aerosols can be measured by aerosol lidars, lidar measurements

55   were used in several campaigns, for example to evaluate the transport of particles (Chazette et al., 2012). Moreover, aerosol lidar networks, such as the European Aerosol Research Lidar Network

(EARLINET), are being developed at *in situ* sites. In space, measurements are performed with the Cloud-Aerosol Lidar with Orthogonal Polarisation (CALIOP) lidar (Winker et al., 2007). Lidar measurements have been used for the validation of aerosol models. For example, Hodzic et al.

60　(2004) compared vertical profiles simulated by CHIMERE with those observed by lidars, from EARLINET, and Stromatas et al. (2012) used observations from the CALIOP space-based lidar. Royer et al. (2011) used an optical-to-mass relationships (urban, pre-urban and rural) to retrieve the PM_{10} (particulate matter with diameter less than 10 µm) concentrations from lidar signals (Raut et al., 2009a,b). In Royer et al. (2011), lidar-derived PM_{10} concentrations were compared with simula-

65　tions from POLYPHEMUS and CHIMERE during the MEGAPOLI (Megacities: Emissions, urban, regional and Global Atmospheric POLlution and climate effects, and Integrated tools for assessment and mitigation) summer experiment in July 2009.

　　Data assimilation (DA hereafter) can reduce the uncertainties in input data such as initial or boundary conditions by coupling models to observations (Bouttier and Courtier, 2002). In air quality,

70　applications of DA to PM_{10} forecast using *in situ* surface measurements have been performed by Denby et al. (2008) and Tombette et al. (2009) over Europe, and Pagowski et al. (2010); Pagowski and Grell (2012); Li et al. (2013) over the United States of America. Over Europe, the efficiency of assimilating lidar measurements to improve PM_{10} forecast has been compared to the efficiency of assimilating *in situ* surface measurements by Wang et al. (2013). Using an Observing System

75　Simulation Experiment (OSSE), they suggested that the assimilation of lidar observations may be more efficient to improve PM_{10} forecast, although it depends on the number of lidar stations used. However, Wang et al. (2013) did not directly assimilate the lidar signal, but they used a relation between mass concentration and optical properties of pollution aerosol. Although this kind of relation has been determined for pollution aerosols over Greater Paris (Raut et al., 2009a), it needs to

80　be generalised to other measurement sites before operationally assimilating the mass concentration converted from the lidar signal. Moreover, the uncertainly linked to the estimation of mass concentrations may be about 25% (Raut et al., 2009a) which is mostly due to uncertainties in estimating the specific cross sections. Because uncertainties in the lidar signal may be less than 5%, it is more accurate to directly assimilate lidar signals.

85　This paper aims at evaluating the lidar signals simulated by POLYPHEMUS and at testing new DA algorithms for assimilating lidar signals. We used measurements performed during the MEGAPOLI summer experiment, when a ground-based mobile lidar (GBLM) was deployed around Paris onboard a van. Measurements from a ground-based *in situ* lidar at Saclay were also performed on 01 July 2009. The evaluation of lidar signals can also be regarded as a preprocessing stage of DA

90　(validation of the observation operator).

　　This paper is organised as follows. Section 2 describes the experiment setup, i.e. the chemistry transport model used (POLYPHEMUS) and the observations. In section 3, the lidar observation operator is presented. Section 4 describes the evaluation of the simulation with *in situ* surface mea-

surements and AERONET data. Results of the comparisons between observed and simulated lidar
signals are shown in section 5. Two new algorithms for the assimilation of lidar observations and
results are shown in section 6. The findings are summarised and discussed in section 7.

2 Experiment setup

2.1 POLAIR3D **model**

In this study, the POLAIR3D air quality model (Sartelet et al., 2007) of the air quality platform
POLYPHEMUS, available at http://cerea.enpc.fr/polyphemus/ and described in Mallet et al. (2007),
is used to simulate air quality over the Greater Paris area. Aerosols are modelled using the SIze-
REsolved Aerosol Model (SIREAM-SuperSorgam), which is described in Debry et al. (2007) and
Kim et al. (2011). SIREAM-SuperSorgam includes 20 aerosol species: 3 primary species (mineral
dust, black carbon and primary organic species), 5 inorganic species (ammonium, sulfate, nitrate,
chloride and sodium) and 12 organic species. Five bins logarithmically distributed over the size
range 0.01 μm - 10 μm are used. The chemical mechanism CB05 (Carbon Bond version 5) is
used for the gas chemistry (Yarwood et al., 2005). POLAIR3D/SIREAM has been used for several
applications. For example, it was compared to *in situ* surface measurements for gas and aerosols
over Europe by Sartelet et al. (2007, 2012); Couvidat et al. (2012), over Greater Paris by Couvidat
et al. (2013), it was compared to AERONET data over Europe by Tombette et al. (2008) and to
satellite data by Zhang et al. (2013), and it was compared to lidar-derived PM_{10} over Greater Paris
during MEGAPOLI by Royer et al. (2011).

2.2 Modelling setup and observational data

The modelling domain is the same as the one used in Royer et al. (2011) and Couvidat et al. (2013).
It covers the Greater Paris area ($[1.2°E, 3.5°E] \times [47.9°N, 50.1°N]$) with a horizontal resolution
of $0.02° \times 0.02°$. Because Royer et al. (2011) show that limited vertical model resolution leads to
much smoother vertical profiles than those deduced from lidar signals, a finer vertical resolution is
used with 23 vertical levels from the ground to 12000 m, instead of nine vertical levels in Royer et al.
(2011). The simulations are carried out for one month from 28 June to 30 July 2009. Meteorological
inputs are the same as in Couvidat et al. (2013). They are simulated with the Weather Research &
Forecasting (WRF) model (Skamarock et al., 2008) using an urban canopy model and an undated
Corine land-use data base (Kim, 2011) with the YSU parameterisation (Hong et al., 2006) for the
Planetary Boundary Layer (PBL) dynamics (Kim et al., 2013). Anthropogenic emissions of gases
and aerosols are generated with the Airparif (the Paris air quality agency) inventory for the year 2005.
Boundary conditions for gaseous and particulate species were obtained from nested simulations over
Europe and France, presented by Couvidat et al. (2013).

The ground based mobile lidar (GBML) used during the MEGAPOLI campaign is based on an

4

ALS450 lidar commercialised by the LEOSPHERE company and initially developed by the Commissariat à l'Energie Atomique (CEA) and the Centre National de la Recherche Scientifique (CNRS) (Chazette et al., 2007). It provides lidar measurements at 355 nm. The main characteristics of this lidar are detailed in Royer et al. (2011). This system is particularly well-adapted to air pollution and tropospheric aerosol studies thanks to its full overlap reached at about 150-200 m height and its increased vertical resolution of 1.5 m. Measurement days of 01, 04, 16, 21, 26 and 29 July 2009, which correspond to different levels of pollution from Airparif (low, moderate or high), are used for comparisons to the lidar signal. Moreover, ground-based *in situ* lidar measurements were performed at Saclay (48.7° N,2.14° E, 30 m a.s.l.) on 01 July 2009 from 06:49 to 16:44 UTC (the blue square in Fig. 1). These measurements are used for both the comparison and the assimilation of lidar observations.

Airparif is the regional operational network in charge of air quality survey around the Paris area (http://www.airparif.asso.fr/). It provides hourly gases and/or aerosol concentrations (PM_{10} and $PM_{2.5}$) measurements. Figure 1 shows the location of the Airparif stations with red squares and/or the black triangles. There are 17 stations at which PM_{10} and/or $PM_{2.5}$ concentration measurements are performed.

The AERONET (AErosol RObotic NETwork) program is a federation of ground-based remote sensing aerosol networks established by NASA and PHOTONS (Univ. of Lille 1, CNES, and CNRS-INSU), which provides a long-term, continuous and readily accessible public domain database of aerosol optical measurements performed by sun-photometers (Holben et al., 1998). Sun-photometers measure AOD at different wavelengths ranging from 340 to 1024 nm. AOD data are computed for three data quality levels: Level 1.0 (unscreened), Level 1.5 (cloud-screened), and Level 2.0 (cloud-screened and quality-assured). The uncertainty of AOD measurements is less than 0.02 (Holben et al., 2001). For this study, there are 2 available stations over Greater Paris: Paris (urban station, 48.87° N, 2.33° E, 50 m a.s.l.) and Palaiseau (suburban station, 48.70° N, 2.21° E, 156 m a.s.l.) (the green discs in Fig. 1). In this paper, Level 2.0 AOD data at 340 and 380 nm are used to derive AOD data at 355 nm following the Angström law:

$$AOD(355) = AOD(340) \left(\frac{355}{340} \right)^{-\alpha}, \tag{1}$$

where α is the Angström exponent defined by

$$\alpha = \ln\left(\frac{AOD(340)}{AOD(380)} \right) / \ln\left(\frac{380}{340} \right). \tag{2}$$

3 Methodology

Figure 2 describes the methodology used for lidar signal modelling from the outputs of the air-quality model and for comparisons to measurements (aerosol concentration measurements, AOD data and lidar vertical profiles). This section presents the methodology used in POLYPHEMUS to derive the lidar observation operator.

5

3.1 Modelling of lidar signals

The range-corrected lidar signal PR_2 measured at an altitude z is defined by Collis and Russell
(1976)

$$\mathrm{PR}_2(z) = C(\beta_m(z) + \beta_a(z)) \exp\left(-2\int_0^z (\alpha_m(z') + \alpha_a(z'))dz'\right), \tag{3}$$

where β_m (resp. β_a) is the molecular (resp. aerosol) backscatter coefficient, α_m (resp. α_a) is the
molecular (resp. aerosol) extinction coefficient, and C is the instrumental constant for each channel
depending on the technical characteristics of the emitting and receiving optics. In order to eliminate
the instrumental constant C (because it is unknown), PR_2 is normalised as follows

$$H(z) = \frac{\mathrm{PR}_2(z)}{\mathrm{PR}_2(z_{\mathrm{ref}})} = \frac{\beta_m(z) + \beta_a(z)}{\beta_m(z_{\mathrm{ref}}) + \beta_a(z_{\mathrm{ref}})} \exp\left(2\int_z^{z_{\mathrm{ref}}} (\alpha_m(z') + \alpha_a(z'))dz'\right), \tag{4}$$

where z_{ref} is taken at an altitude in the molecular zone. In equation (4), to estimate the normalised
lidar signal H, four optical parameters β_m, β_a, α_m and α_a are needed.

The molecular backscatter coefficient (β_m) at the wavelength λ of the incident light is calculated
by Nicolet (1984)

$$\beta_m = \frac{P}{k_{\mathrm{B}}T} \cdot s_{\mathrm{Ray}}, \tag{5}$$

where P is the pressure, T is the temperature, k_{B} is the Boltzmann constant, and the Rayleigh
scattering cross section s_{Ray} is given by

$$s_{\mathrm{Ray}} = 4.678 \cdot 10^{-29} \cdot \lambda^{-(3.916 + 0.074 \cdot \lambda + 0.05/\lambda)}. \tag{6}$$

The molecular extinction coefficient (α_m) is given by Nicolet (1984)

$$\alpha_m = \frac{8\pi}{3}\beta_m. \tag{7}$$

Aerosol extinction and backscatter coefficients (β_a and α_a) are functions of the particle sizes, of
the aerosol complex refractive index (ACRI) of particles m, and of the wavelength λ of the incident
light. With a population of different-sized particles of identical refractive index m and with a number
size distribution function $n(D_{\mathrm{wet}})$ with D_{wet} the particle wet diameter, the aerosol extinction and
backscatter coefficients are given by the following formulas:

$$\alpha_a = \int_0^{D_{\mathrm{wet}}^{\max}} \frac{\pi D_{\mathrm{wet}}^2}{4} Q_{\mathrm{ext}}(m, a_{\mathrm{wet}}) n(D_{\mathrm{wet}}) dD_{\mathrm{wet}}, \tag{8}$$

and

$$\beta_a = \int_0^{D_{\mathrm{wet}}^{\max}} \frac{\pi D_{\mathrm{wet}}^2}{4} Q_{\mathrm{bsca}}(m, a_{\mathrm{wet}}) n(D_{\mathrm{wet}}) dD_{\mathrm{wet}}, \tag{9}$$

where $D_{\mathrm{wet}}^{\max}$ is a wet diameter upper limit for the particle population, $a_{\mathrm{wet}} = \frac{\pi D_{\mathrm{wet}}}{\lambda}$ a dimension-
less size parameter, $Q_{\mathrm{ext}}(m, a_{\mathrm{wet}})$ and $Q_{\mathrm{bsca}}(m, a_{\mathrm{wet}})$ are extinction and backscatter efficiencies.
These efficiencies are computed through the Mie code from ftp://ftp.giss.nasa.gov/pub/crmim/spher.f

6

(de Rooij and van der Stap, 1984; Mishchenko et al., 2002). The dry complex refractive index (CRI) is interpolated from the OPAC package (Hess et al., 1998) for each species at the desired wavelength λ (355 nm). The CRI and densities used for calculation of optical properties are shown in Table 1. The wet diameter D_{wet} is computed from the mean dry diameter of each section of the aerosol sectional model SIREAM and from the aerosol water content. The aerosol water content is calculated from the thermodynamic model ISORROPIA (Nenes et al., 1998a,b) which models the phase state (i.e. gas, liquid, solid) of inorganic aerosol species (i.e. ammonium, sodium, chloride, nitrate, sulfate) in equilibrium with gaseous precursors. The inputs of ISORROPIA are temperature, relative humidity (RH), gaseous precursor concentrations and inorganic aerosol concentrations. Because of the large amount of water vapour in the atmosphere, the ambient RH is assumed to be unaffected by the deliquescence of aerosol particles in ISORROPIA (Nenes et al., 1998a) and equals the water activity (referred to as a_w). The aerosol water content is estimated by the ZSR relationship (Robinson and Stokes, 2002),

$$W = \sum_i \frac{M_i}{m_{oi}(a_w)}, \tag{10}$$

where $a_w =$RH, W is the aerosol water content concentration, M_i is the molar concentration of species i (mol m^{-3}), $m_{oi}(a_w)$ is the molality of an aqueous solution of species i (mol kg^{-1}).

Computing the ACRI requires to make an assumption on the mixing state of the aerosol chemical species. The current version of POLYPHEMUS is based on an assumption of aerosol internal mixing: all the particles of a given size section at a given grid point of the domain are supposed to have the same chemical composition. Within this framework, Tombette et al. (2008) compared aerosol optical properties using 2 different assumptions for the Black Carbon (BC) mixing state: internally homogeneous mixing and core-shell mixing. In the internally homogeneous mixing case, BC is treated as the other components and a volume-weighted ACRI is calculated from the CRI of pure species. In the core-shell mixing case, each particle is assumed to have a structure : the core (BC) and the shell (all the other components). The hypothesis of an internally homogeneous mixing state seems to be unphysical as BC can not be well-mixed in the particle because of its complex geometry and solid state (Katrinak et al., 1993; Sachdeva and Attri, 2007). Tombette et al. (2008) have shown that the use of these two mixing states leads to negligible differences on AOD, but non-negligible differences on single scattering albedo and absorption process. According to illustrations of Jacobson (2000), the BC mixing state influences the absorption cross section at small wavelengths (lower than 1 μm) for aerosols with diameter higher than 1 μm. Thus, a core-shell mixing hypothesis is used in this study. The Maxwell-Garnett approximation is used to calculate ACRI from the core CRI (i.e., BC in this study) and the shell CRI (where all the other components are well mixed) (Tombette et al., 2008).

3.2 Estimation of z_{ref}

The altitude used to normalise the lidar signal does not need to correspond exactly to the beginning altitude of the molecular zone, but it could be any arbitrary chosen altitude in the molecular zone, where there is almost no aerosol. However, it is better to use an estimation of the normalisation altitude as close as possible to the beginning of the molecular zone, because lidar signals are attached to higher uncertainties at high altitudes because of a higher signal-to-noise ratio. Although the molecular zone is often determined visually from lidar vertical profiles, this method is not efficient to treat large amounts of lidar profiles. We therefore created a new algorithm which can automatically estimate the normalisation altitude z_{ref} from the lidar vertical profile.

The normalisation altitude z_{ref} is estimated from the lidar signal and the simulated molecular signal $\mathrm{PR}_{2,\mathrm{Ray}}$

$$\mathrm{PR}_{2,\mathrm{Ray}}(z) = \beta_m(z)\exp\left(-2\int_0^z \alpha_m(z')dz'\right), \tag{11}$$

as follows :

- Define a weight for each vertical point of the lidar signal (the vertical resolution is 1.5 m). The weights should be larger for the points that are more likely to be in the molecular zone, i.e. at high altitudes. We used $w(h) = \exp((h - h_{\mathrm{max}})/L)/L$, where h is the altitude of the points, h_{max} is the maximal altitude considered (e.g. 4 km) and the parameter L is taken equal to 200 m.

- Fit all lidar signal vertical points (noted as a vector $\mathbf{y}$) with a weighted least absolute deviations (LAD) regression (DasGupta and Mishra, 2007). It is because we are here interested in the linear regression of lidar signal points at higher altitudes, e.g. the points between 2 and 3 km above the ground. However, it is difficult to know the altitude below which lidar signal points could be cut off for the estimation of z_{ref}. When considering all available lidar signal points, the disturbances are prominently non-normally distributed and contain sizeable outliers (i.e. points at lower altitudes). In such cases, the Least Squares method fails and the LAD method performs well (DasGupta and Mishra, 2007). In detail, we minimise

$$\|(\mathbf{y} - (a\mathbf{h} + b))^{\mathrm{T}}\mathbf{w}\|_{l1} = \sum_i |w_i(y_i - ah_i - b)| \tag{12}$$

to find a and b (cyan lines in Fig. 3).

- Calibrate the simulated molecular signal $\mathrm{PR}_{2,\mathrm{Ray}}$ with the LAD regression line at altitude h_{max}, and calculate the difference between the calibrated $\mathrm{PR}_{2,\mathrm{Ray}}$ and the LAD regression line at each vertical point of the lidar signal in a loop starting from high altitudes to low altitudes. The altitude at which the difference becomes larger than a pre-assigned value (1% of the value corresponding to the LAD regression line) corresponds to z_{ref}.

8

260   Figure 3 shows comparisons between the lidar signal and the simulated molecular signal $\mathrm{PR}_{2,\mathrm{Ray}}$
for different lidar measurement days during MEGAPOLI. The simulated molecular signal (red lines
in Fig. 3) agrees well with the lidar observations (black lines in Fig. 3) at high altitudes in the
molecular zone, leading to the determination of the molecular zone and z_{ref}.

4   Model evaluation

265   To evaluate air quality models, Boylan and Russell (2006) recommended PM model performance
goal and criterion that are based upon an analysis of numerous PM and visibility modelling studies.
The PM model performance goal corresponds to the level of accuracy that is considered to be close
to the best a model can be expected to achieve. The PM model performance criterion corresponds
to the level of accuracy that is considered to be acceptable for modelling applications. The Mean
270   Fractional Bias (MFB) and the Mean Fractional Error (MFE) are proposed by Boylan and Russell
(2006) to evaluate model performances against observations: if both the MFB is in the range [-30
%, 30%] and the MFE is in the range [0, 50 %], the PM model performance goal is met; if both the
MFB is in the range [-60 %, 60%] and the MFE is in the range [0, 75 %], the PM model performance
criterion is met. RMSE and correlation are also often used in the aerosol modelling community. The
275   statistical indicators are defined in appendix A.

4.1   Model evaluation with Airparif data

Table 2 shows statistics for the month of simulation and for the 6 lidar measurement days. For the
month of simulation, for $PM_{2.5}$, the MFB and MFE are respectively in the range [-30 %, 30%] and
[0, 50 %], i.e. the PM model performance goal is met. For PM_{10}, the MFB and MFE are respectively
280   in the range [-60 %, 60%] and [0, 75 %], i.e. the PM model performance criterion is met. For each
lidar measurement day, the PM model performance goal is always met for $PM_{2.5}$, and the PM model
performance criterion is met for PM_{10} except for 29 July.

As shown in Table 2, the model simulates well $PM_{2.5}$ concentrations, but PM_{10} concentrations
are underestimated. In other words, coarse particles (particulate matter with a diameter higher than
285   2.5 µm and lower than 10 µm) are underestimated. This may be because emissions and boundary
conditions of coarse particles are underestimated, e.g. road resuspensions of PM is not considered
in the model and boundary conditions are obtained from nested simulations over Europe and France
where coarse particles were underestimated.

4.2   Model evaluation with AERONET data

290   Table 3 presents statistics for hourly data. As the MFB and MFE on 01, 04, 16 and 26 July 2009 are
respectively in the range [-60 %, 60%] and [0, 75 %], the model performance criterion of Boylan
and Russell (2006) is met, despite a slight underestimation of AOD in agreement with the underes-

timation of PM_{10} in comparison to Airparif observations (see section 4.1).

5 Comparisons with lidar vertical profiles

295   The simulated lidar signal is compared with GBML observations performed during the MEGAPOLI summer experiment on the different measurement days (01, 04, 16, 21, 26 and 29 July 2009). The purpose of this section is to validate the ability of POLYPHEMUS to simulate lidar backscattered profiles and then choose suitable measurement days to do assimilation tests.

On 01 July 2009, GBML measurements are performed leeward inside the pollution plume in the
300   Southwest of Paris between Saclay and Chateaudun during 3 hours (black track in Fig. 1). It is the most polluted day of the MEGAPOLI experiment. High levels of PM_{10}, on average about 45 $\mu g\, m^{-3}$ (see Tab. 2), are measured by the Airparif network. Figure 4 presents the comparison between lidar observations and the simulation at 11:00 , 12:00 and 13:00 UTC. It shows that POLYPHEMUS underestimates the lidar signal at 13:00 UTC, but it overestimates it at 14:00 UTC and it agrees well
305   with observations at 15:00 UTC. While the PBL height increases from about 1.2 to 1.8 km from 11:00 to 13:00 UTC and the GBML runs out of the pollution plume (Royer et al., 2011), both the observed and simulated lidar signals decrease. Figures of the comparison between the simulation and observations from a ground-based *in situ* lidar at Saclay are shown later in this paper. The pollution plume covers Saclay because of the Northeast wind. Thus high lidar signal values in both
310   the simulation and observations are seen after 10:00 UTC, although the simulated lidar signals are underestimated. Data assimilation will be performed for this day, as it is the most polluted day with observations from both the GMBL and a ground-based in situ lidar.

On 04 July 2009, GBML measurements are performed around Paris with a circular pattern from 14:49 to 17:24 UTC. Particle AOD and concentrations are underestimated in the simulation. The
315   daily averaged AOD from the AERONET network is about 0.25, respectively 0.14 in the simulation (see Tab. 3). The daily averaged PM_{10} concentration from the Airparif network is about 18.37 $\mu g\, m^{-3}$, respectively 11.11 $\mu g\, m^{-3}$ in the simulation (see Tab. 2). Figure 5 shows the comparison between the GBML measurements and the simulation at 15:03 UTC and 16:00 UTC. The simulated lidar signals are underestimated. Moreover, lidar measurements show an aerosol layer between 2.0
320   km and 3.0 km (probably from long-range transport), which is not present in the simulation, but impacts the lidar signal until low altitudes. It is mostly because boundary conditions do not provide information about this aerosol layer due to the large-scale model uncertainties.

On 16 July 2009, GBML measurements are performed in the North of Paris from Saclay to Amiens between 11:00 UTC and 14:30 UTC. The lidar signal is overall underestimated, as shown
325   in Fig. 6, in agreement with the underestimation of PM_{10} shown by the statistics in Tables 2 and 3. Surface PM_{10} concentration from the Airparif network and from the simulation are respectively 26.25 and 16.47 $\mu g\, m^{-3}$ (low-moderate level of pollution, see Tab. 2). The observed and simulated

10

AOD are respectively 0.26 and 0.18 (see Tab. 3). The simulated AOD has a good correlation with AERONET data (up to 80 %). As deduced from the comparisons of the modelled and observed lidar signals in Fig. 6, the PBL height is well modelled until 12:00 UTC, but it is underestimated afterwards, e.g. the PBL height is about 2.1 km from the observed lidar signal but it is about 1.6 km in the simulation. These differences in PBL height explain that the simulated lidar signal agrees better with the observation until 12:00 UTC.

On 21 July 2009, the GBML travels from Saclay to the North of Paris across the city centre of Paris. As shown in Fig. 7, the lidar signal is overestimated for this measurement day. However, the surface PM_{10} concentration is underestimated. It is 27.84 and 16.84 $\mu g\,m^{-3}$ (low-moderate level of pollution, see Tab. 2) from the Airparif network and from the simulation respectively. The large simulated lidar signals originate in high aerosol concentration at high altitudes, i.e. between 2.0 km and 2.5 km, which leads to higher backscattering and extinction coefficients. This high-altitude aerosol layer originates in boundary conditions (large-scale model uncertainties), but it is not present in the observations. It impacts the lidar signal until low altitudes. This is why surface PM_{10} is underestimated while lidar signal is overestimated.

On 26 July 2009, the GBML followed two circular patterns (the yellow and cyan tracks in Fig. 1). One is performed from 12:40 to 15:30 UTC at a distance between 15 and 30 km from the city centre. Another one is performed from 16:44 to 18:18 UTC in the South-Southwest of Paris. Low levels of pollution are observed and simulated. Surface PM_{10} concentration and AOD are underestimated. The daily averaged PM_{10} concentration from Airparif is 18.04 $\mu g\,m^{-3}$, against 10.12 $\mu g\,m^{-3}$ in the simulation. The mean observed AOD value is 0.15, against 0.08 in the simulation. Although the lidar signal is slightly underestimated in the simulation, simulated and observed lidar signals agree fairly well, as shown in Figure 8. The pollution from Paris is transported by the South wind to the North. This is why the lidar signal is higher at 14:00 UTC in Fig. 8. Because as much as 5 hours of lidar measurements are performed, which is longer than on 04, 16, 21 and 29 July 2009, we will perform data assimilation for this day.

On 29 July 2009, GBML measurements are performed from 12:22 to 15:10 UTC in the North of Paris and in peri-urban and rural areas. While low levels of pollution (12.33 $\mu g\,m^{-3}$ of the mean PM_{10} concentration in Tab. 2) are simulated, moderate levels of pollution (29.25 $\mu g\,m^{-3}$ of the mean PM_{10} concentration in Tab. 2) is observed by the Airparif network. As deduced from Figure 9, at the beginning of measurement period, the PBL height is about 1.5 km and the simulated lidar signal agrees well with the lidar observations. At 15:00 UTC, the observed lidar signal has increased, because of an aerosol layer between 2.0 and 3.5 km. This layer is not simulated and the simulated lidar signal is underestimated.

For all measurement days, we also computed the statistics (i.e. RMSE, correlation, MFB and MFE) between observed and simulated lidar vertical profiles. The scores are shown respectively in Figures 4, 5, 6, 7, 8 and 9. Overall, RMSEs are below 1.63, the MFB ranges from -38 % to 8 % and

11

365 the MFE ranges from 3 % to 38 %. Currently, there is no criterion to evaluate the comparisons for lidar signals. The criterion of Boylan and Russell (2006) was designed for PM concentration and light extinction. Because the scores of the lidar signal comparisons are extremely good compared to the criterion of Boylan and Russell (2006) with low errors and bias, the criterion of Boylan and Russell (2006) may not be restrictive enough for lidar signals.

370 ## 6 Assimilation test of lidar observations

DA of lidar observations is performed for two out of the six different measurement days. Only two days are retained because the other days were cloudy and our algorithms do not allow us to assimilate lidar data when there are clouds. There are 13 h of cloud-cleaned measurements on 01 July, 5 h of cloud-cleaned measurements on 26 July and less than 3 h of cloud-cleaned measurements on the
375 other measurement days. Therefore, DA run is performed on 01 and 26 July 2009 because too few data are available during the other measurement days.

In air quality, the large number of state variables leads to high computational costs when implementing DA algorithms. Among the widely used DA algorithms, the optimal interpolation (OI) is used here, as it is the most computationally efficient (Denby et al., 2008; Tombette et al., 2008;
380 Wu et al., 2008; Li et al., 2013). In applications of DA to aerosol forecast, Tombette et al. (2009) have used the OI over western Europe for assimilating observations from the BDQA network, which covers France. Denby et al. (2008) have used two different DA techniques, the OI and EnKF, to assimilate PM_{10} concentrations over Europe. Pagowski et al. (2010) have used the OI over the United States of America for data assimilation of $PM_{2.5}$ observations. Li et al. (2013) have used the OI
385 for multiple aerosol species and for prediction of $PM_{2.5}$ in the Los Angeles basin. And Wang et al. (2013) have used the OI over Europe to investigate the potential impact of future ground-based lidar networks on analysis and short-term forecasts of PM_{10}.

6.1 Basic formulation

A simple formulation for DA of lidar signals with OI is now described. Particles are represented
390 in the model by mass concentrations of different chemical species for the different particle size sections.

The state vector $\mathbf{x}$ is defined by

$$\mathbf{x} = \{x_{i,j,k}^h\}_{1 \leq i \leq N_b, 1 \leq j \leq N_s, 1 \leq k \leq n, 1 \leq h \leq l}, \tag{13}$$

where $x_{i,j,k}^h$ is the mass concentration of the aerosol species j in section i for the horizontal spatial
395 grid k at the model vertical level h, N_b is the number of size sections, N_s is the number of chemical species, n is the number of horizontal grid points at each vertical level h and l is the total number of vertical levels.

The analysed state vector is a solution to the variational optimisation problem:

$$\mathbf{x}^a = \operatorname{Argmin} \ J(x), \tag{14}$$

where J is the cost function defined by

$$
\begin{aligned}
J(\mathbf{x}) &= \frac{1}{2}\left(H(\mathbf{x}) - \mathbf{y}\right)^{\mathrm{T}} \mathbf{R}^{-1}\left(H(\mathbf{x}) - \mathbf{y}\right) + \frac{1}{2}\left(\mathbf{x} - \mathbf{x}^b\right)^{\mathrm{T}} \mathbf{B}^{-1}\left(\mathbf{x} - \mathbf{x}^b\right) \\
&\simeq \frac{1}{2}\left(H(\mathbf{x}^b) + \mathbf{LS}(\mathbf{x} - \mathbf{x}^b) - \mathbf{y}\right)^{\mathrm{T}} \mathbf{R}^{-1}\left(H(\mathbf{x}^b) + \mathbf{LS}(\mathbf{x} - \mathbf{x}^b) - \mathbf{y}\right) \\
&\quad + \frac{1}{2}\left(\mathbf{x} - \mathbf{x}^b\right)^{\mathrm{T}} \mathbf{B}^{-1}\left(\mathbf{x} - \mathbf{x}^b\right),
\end{aligned}
\tag{15}
$$

where $\mathbf{x}^b$ is the model concentrations, $\mathbf{y}$ is the vector of observations, $H(\mathbf{x}) = \mathbf{L} \cdot S(\mathbf{x})$ is the lidar observation operator, S is a nonlinear operator from the model state $\mathbf{x}$ to the lidar signal state, $\mathbf{L}$ is a linear spatial interpolation operator, $\mathbf{S}$ is the tangent linear of operator S, $\mathbf{B}$ and $\mathbf{R}$ are the matrices of error covariances for backgrounds and observations respectively. In this way, we have

$$\nabla J(\mathbf{x}^a) = (\mathbf{LS})^{\mathrm{T}} \mathbf{R}^{-1}\left(H(\mathbf{x}^b) - \mathbf{y}\right) + \left(\mathbf{B}^{-1} + (\mathbf{LS})^{\mathrm{T}} \mathbf{R}^{-1}(\mathbf{LS})\right)\left(\mathbf{x}^a - \mathbf{x}^b\right) = 0, \tag{16}$$

which leads to

$$
\begin{aligned}
\mathbf{x}^a - \mathbf{x}^b &= \left(\mathbf{B}^{-1} + (\mathbf{LS})^{\mathrm{T}} \mathbf{R}^{-1}(\mathbf{LS})\right)^{-1}\left(\mathbf{y} - H(\mathbf{x}^b)\right) \tag{17} \\
&= \mathbf{B}(\mathbf{LS})^{\mathrm{T}}\left((\mathbf{LS})\mathbf{B}(\mathbf{LS})^{\mathrm{T}} + \mathbf{R}\right)^{-1}\left(\mathbf{y} - H(\mathbf{x}^b)\right). \tag{18}
\end{aligned}
$$

6.2 Construction of error covariances

Since the measurements at different levels originate from the same lidar, the matrix $\mathbf{R}$ should not be diagonal because of measurement error correlations. However, in order to simplify $\mathbf{R}$ in the first tests of DA of lidar observations, one takes $\mathbf{R} = r\mathbf{I}$ as a diagonal matrix where $\mathbf{I}$ is the identity matrix and r is an error variance. The value of the observation error variance r is determined by a χ^2 diagnosis (Ménard et al., 1999), in which the scalar

$$\chi^2 = \left(\mathbf{y} - H(\mathbf{x}^b)\right)^{\mathrm{T}}\left((\mathbf{LS})\mathbf{B}(\mathbf{LS})^{\mathrm{T}} + \mathbf{R}\right)^{-1}\left(\mathbf{y} - H(\mathbf{x}^b)\right) \tag{19}$$

should be equal, on average, to the number of observations (N) at each DA step.

Specifically, $\mathbf{B}$ plays a role in determining how the corrections of the concentrations should be distributed over the domain during DA. In practice, however, it is impossible to accurately know all coefficients of $\mathbf{B}$. In our simulation, the number of model grid points is of the order of 10^5. Thus the number of coefficients in the matrix $\mathbf{B}$ is about 10^{10} multiplied by the square of the number of analysis variables (about 100 variables for particles are used here). Therefore, $\mathbf{B}$ is too large to be handled numerically.

In order to reduce the size of the error covariance matrices for background, we model the matrix $\mathbf{B}$ as follows

$$\mathbf{B} = \mathbf{PDP}^{\mathrm{T}}, \tag{20}$$

13

where $\mathbf{D}$ is the error covariance matrix for PM_{10}, defined by the Balgovind approach (Balgovind et al., 1983) obtained by considering the RMSE and correlation of simulated PM_{10} concentrations. Thus, the size of $\mathbf{D}$ is much less than the one of $\mathbf{B}$. The matrix $\mathbf{P}$ is defined by

$$\mathbf{P} = \begin{bmatrix} \mathbf{v}_1 & \mathbf{0} & \dots & \mathbf{0} \\ \mathbf{0} & \mathbf{v}_2 & \dots & \mathbf{0} \\ \vdots & \vdots & \ddots & \vdots \\ \mathbf{0} & \mathbf{0} & \dots & \mathbf{v}_M \end{bmatrix}_{(M \cdot N_b \cdot N_s) \times M},$$

where M is equal to the dimension of the domain $(l \cdot n)$, $\mathbf{v}_k$ is a vector of size $N_b \cdot N_s$ (the number of state variables). Each component of $\mathbf{v}_k$ corresponds to the proportion of the mass of particles for a given species in a given size section in PM_{10} mass concentrations at grid point k.

Let $\mathbf{S}' = \mathbf{SP}$ be the directional derivative of S along a given direction, and let $\mathbf{c}^b$ and $\mathbf{c}^a$ be PM_{10} concentration states before and after analysis respectively. In order to convert $\mathbf{x}$ into the PM_{10} state $\mathbf{c}$, we multiply each side of equation (18) by the matrix $\mathbf{Z}$:

$$\mathbf{Z} = \begin{bmatrix} 1 & \dots & 1 & 0 & \dots & 0 & 0 & \dots & 0 & 0 & \dots & 0 \\ 0 & \dots & 0 & 1 & \dots & 1 & 0 & \dots & 0 & 0 & \dots & 0 \\ \vdots & \ddots & \vdots & \vdots & \ddots & \vdots & \vdots & \ddots & \vdots & \vdots & \ddots & \vdots \\ 0 & \dots & 0 & 0 & \dots & 0 & 0 & \dots & 0 & 1 & \dots & 1 \end{bmatrix}_{M \times (M \cdot N_b \cdot N_s)}.$$

We obtain

$$\mathbf{c}^a - \mathbf{c}^b = \mathbf{D}(\mathbf{LS}')^{\mathrm{T}} \left((\mathbf{LS}')\mathbf{D}(\mathbf{LS}')^t + \mathbf{R} \right)^{-1} \left(\mathbf{y} - H(\mathbf{x}^b) \right). \tag{21}$$

After the analysis, the concentrations $\mathbf{c}^a$ are redistributed over particle species and size sections following the initial chemical and size distributions.

6.3 DA setup

DA experiments are carried out for 01 and 26 July 2009. All DA experiments are performed with a time step of 600 s and from 200 to 1800 m above the ground (10 model levels), since the lidar measurements are not available below the altitude of full overlap (200 m above the ground) and since aerosol concentrations above the PBL have limited impact on surface PM_{10} in the short term (Wang et al., 2013). In the Balgovind approach (Balgovind et al., 1983), the horizontal correlation length is set to $0.2°$, which is estimated from numerical DA tests. The error variances are separately set for each DA level, depending on the RMSE of PM concentrations and the variability of PM concentrations at each model level.

Two new algorithms are tested for the assimilation of lidar observations. In the first algorithm, we use the assimilation of lidar observations to analyse PM_{10} concentrations and the analysed PM_{10} concentrations are redistributed over particle species and size sections following the initial chemical and size distributions (see section 6.2). The background error variances of PM_{10} concentrations are

14

estimated by the simulation without DA and Airparif observations. The value of the observation error variance r is determined by a χ^2 diagnosis, which yields $r = 1$ $\mu g^2\,m^{-6}$ and $r = 0.006$ $\mu g^2\,m^{-6}$ respectively for 01 and 26 July, depending on the level of uncertainties (see section 5). Let N be the number of lidar observations at one DA step. Figure 10 shows the time evolution of χ^2/N (blue lines) for DA runs on 01 and 26 July. The mean over DA window of χ^2/N is 1.02 (resp. 1.02) for 01 (resp. 26) July.

In the second algorithm, we separately analyse $PM_{2.5}$ and $PM_{2.5-10}$ (particulate matter with a diameter higher than 2.5 μm and lower than 10 μm) in the assimilation of lidar observations. We modify the matrices used in section 6.2 to obtain $\mathbf{c_{2.5}}$ and $\mathbf{c_{2.5-10}}$, the mass concentrations of $PM_{2.5}$ and $PM_{2.5-10}$ respectively (see Appendix B for details). We separately set the error variances for $PM_{2.5}$ and $PM_{2.5-10}$ in matrix $\mathbf{D}$. Because of the lack of $PM_{2.5-10}$ observations, we can not directly estimate the background error variances. They are determined by the χ^2 diagnosis using the observation error variance r found in the first algorithm.

In the following, we note the assimilation with the first (resp. second) DA algorithm as "DA (PM_{10})" (resp. "DA ($PM_{2.5}$ and $PM_{2.5-10}$)").

6.4 Results and discussions

In these DA tests, the purpose is to verify if these new algorithms are functional. Because we work at small scale, the corrections of DA are transported out of the simulation domain very quickly. Thus we only compute the statistics for the DA window to validate the DA tests.

Table 4 presents statistics of the simulation results without DA and with DA. Statistics are computed for both PM_{10} and $PM_{2.5}$ concentrations. Overall, both DA algorithms lead to better scores (lower RMSE, MFB and MFE, and higher correlation) than the simulation without DA for PM_{10} concentrations. Comparing the two DA algorithms, the simulation with DA ($PM_{2.5}$ and $PM_{2.5-10}$) leads to better scores than the simulation with DA (PM_{10}) for PM_{10} concentrations (see Tab. 4). The RMSE of PM_{10} is 11.63 $\mu g\,m^{-3}$ in the simulation with DA ($PM_{2.5}$ and $PM_{2.5-10}$), against 13.69 $\mu g\,m^{-3}$ in the simulation with DA (PM_{10}) on 01 July. The RMSE of PM_{10} is 4.73 $\mu g\,m^{-3}$ in the simulation with DA ($PM_{2.5}$ and $PM_{2.5-10}$), against 6.08 $\mu g\,m^{-3}$ in the simulation with DA (PM_{10}) on 26 July. It is because higher background error variances are set for the coarse sections in the simulation with DA ($PM_{2.5}$ and $PM_{2.5-10}$). However, the simulation with DA ($PM_{2.5}$ and $PM_{2.5-10}$) leads to similar scores to the simulation with DA (PM_{10}) for $PM_{2.5}$ concentrations (see Tab. 4). It is because similar background error variances for $PM_{2.5}$ in the simulation with DA ($PM_{2.5}$ and $PM_{2.5-10}$) to the simulation with DA ($PM_{2.5}$) are used in the χ^2 diagnosis, since fine particles contribute to more than 80% of the lidar signal (Randriamiarisoa et al., 2006). In the following, we compare the simulation without DA and the simulation with DA ($PM_{2.5}$ and $PM_{2.5-10}$).

On 01 July, the averaged RMSE of PM_{10} is 11.63 $\mu g\,m^{-3}$ with DA ($PM_{2.5}$ and $PM_{2.5-10}$), against 17.74 $\mu g\,m^{-3}$ without DA. The decrease of the RMSE are explained by the correlation length in the

matrix $\mathbf{D}$, since no Airparif station performs measurements in the Southwest of Paris (the Northeast wind). At station *Issy-Les-Moulineaux* (48.82° N, 2.27° E, 36 m a.s.l.), the closest station to Saclay, the RMSE of PM_{10} is 14.72 $\mu g\,m^{-3}$ with DA ($PM_{2.5}$ and coarse), against 22.81 $\mu g\,m^{-3}$ without DA. However, the averaged RMSE of $PM_{2.5}$ is about 10.4 $\mu g\,m^{-3}$ with DA ($PM_{2.5}$ and $PM_{2.5-10}$), against 8.54 $\mu g\,m^{-3}$ without DA. This is due to the larger horizontal correlation length (see section 6.3). While DA runs increase PM concentrations in the lidar measurement grids, PM concentrations are increased at Airparif stations, where $PM_{2.5}$ concentrations is well simulated and coarse particles are underestimated. This problem can be solved by decreasing the horizontal correlation length. Figure 11 shows that the model underestimates the lidar signal at Saclay. The simulation with DA simulates better the lidar signal than the one without DA. It means that DA corrects well the model aerosol concentrations (the closer to the truth the model aerosol concentrations are, the better the lidar signals are simulated).

On 26 July, the averaged RMSE of PM_{10} is 4.73 $\mu g\,m^{-3}$ with DA ($PM_{2.5}$ and $PM_{2.5-10}$), against 6.67 $\mu g\,m^{-3}$ without DA. Because two circular GBML travelling patterns were performed around Paris (see Fig. 1), most of Airparif stations are leeward (the South wind) or they are close to the patterns of GBML. They could validate improvements of PM concentrations. At station *Paris 1er Les Halles* (48.86° N, 2.35° E, 35 m a.s.l.), the RMSE of PM_{10} is 1.96 $\mu g\,m^{-3}$ in the simulation with DA ($PM_{2.5}$ and $PM_{2.5-10}$), against 4.71 $\mu g\,m^{-3}$ in the simulation without DA. Moreover, DA runs lead to better scores than the simulation without DA for $PM_{2.5}$. At leeward station *Creil Faiencerie* (49.26° N, 2.47° E, 28 m a.s.l.), the RMSE of $PM_{2.5}$ is 4.1 $\mu g\,m^{-3}$ in the simulation with DA ($PM_{2.5}$ and $PM_{2.5-10}$), against 4.9 $\mu g\,m^{-3}$ in the simulation without DA.

7 Conclusions

In order to investigate the ability of the CTM POLAIR3D of the air quality modelling platform POLYPHEMUS to simulate lidar vertical profiles, we performed a simulation over the Greater Paris area for the summer month of July 2009. The results (PM_{10} and $PM_{2.5}$ concentrations) are evaluated using Airparif data. We simulated aerosol optical properties and lidar signals from the model aerosol concentration outputs using the aerosol complex refractive index (ACRI) and the wet particle diameter. The AOD was evaluated using AERONET data: the RMSE ranges from 0.07 to 0.20, the MFB ranges from -58 % to -21 % and the MFE ranges from 29 % to 58 %. According to the criterion of Boylan and Russell (2006), the model performance criterion is met for AOD. Hourly comparisons between simulated lidar signals and lidar observations were described for six measurement days during the MEGAPOLI summer campaign. These comparisons showed a good agreement between GBML measurements and the simulation except for 04 July 2009, where an aerosol layer was not modelled at high altitudes but observed in lidar measurements, and for 21 July 2009, where an aerosol layer was modelled at high altitudes but not observed in lidar measurements.

The statistics obtained for the lidar comparison are extremely good compared to the criterion of Boylan and Russell (2006) with low errors and bias: the MFB ranges from -38 % to 8 % and the MFE ranges from 3 % to 38 %. Because the criterion of Boylan and Russell (2006) was designed for PM concentration and light extinction, they may not be restrictive enough for lidar signals. A specific criterion would therefore need to be designed. Overall, the results show that the optical property module of POLYPHEMUS models well lidar signals.

Two new algorithms for the assimilation of lidar observations based on the optimal interpolation method were presented. One algorithm analyses PM_{10} concentrations. Another analyses $PM_{2.5}$ and $PM_{2.5-10}$ concentrations separately. DA tests were performed for only 01 and 26 July 2009, because the other measurement days were cloudy and our algorithms do not allow us to assimilate lidar data when there are clouds. Both of these algorithms lead to better scores (lower RMSE, MFB and MFE, and higher correlation) for PM_{10} and $PM_{2.5}$ on 26 July 2009. However, they did not improve $PM_{2.5}$ on 01 July 2009, because of the large horizontal correlation length. The simulation with DA ($PM_{2.5}$ and $PM_{2.5-10}$) leads to better scores than the simulation with DA (PM_{10}) because the error variances for backgrounds are set separately for fine ($PM_{2.5}$) and coarse ($PM_{2.5-10}$) particles. The results shown in this paper suggest that the assimilation of lidar observations that analyses $PM_{2.5}$ and $PM_{2.5-10}$ would perform better than the assimilation of lidar observations that analyses PM_{10}, but it is computationally more costly.

Comparing the simulation without DA and the simulation with DA ($PM_{2.5}$ and $PM_{2.5-10}$), the averaged RMSE of PM_{10} is 11.63 $\mu g\,m^{-3}$ with DA ($PM_{2.5}$ and $PM_{2.5-10}$), against 17.74 $\mu g\,m^{-3}$ without DA on 01 July 2009. The averaged RMSE of PM_{10} is 4.73 $\mu g\,m^{-3}$ with DA ($PM_{2.5}$ and $PM_{2.5-10}$), against 6.67 $\mu g\,m^{-3}$ without DA on 26 July 2009.

A forthcoming paper will present results about the assimilation of continuous measurements from the ACTRIS/EARLINET network during a 72-hour period of intensive observations.

Appendix A   Statistical indicators

$\{o_i\}_{i=1,n}$ and $\{s_i\}_{i=1,n}$ are the observed and the modelled concentrations at time i, respectively. n is the number of available observations. The statistical indicators used to evaluate the results with respect to observations are: the Root Mean Square Error (RMSE), the (Pearson) correlation, the Mean Fractional Error (MFE), the Mean Fractional Bias (MFB). MFE and MFB bound the maximum error and bias and do not allow a few data points to dominate the statistics. They are

often used to evaluate model performances against observations for aerosol mass concentrations and optical properties (Boylan and Russell, 2006). The statistical indicators are defined as follow:

$$\text{RMSE} = \sqrt{\frac{1}{n}\sum_{i=1}^{n}(o_i - s_i)^2}, \tag{A1}$$

$$\text{correlation} = \frac{\sum_{i=1}^{n}(o_i - \bar{o})(s_i - \bar{s})}{\sqrt{\sum_{i=1}^{n}(o_i - \bar{o})^2 \sum_{i=1}^{n}(s_i - \bar{s})^2}}, \tag{A2}$$

$$\text{MFE} = \frac{1}{n}\sum_{i=1}^{n}\frac{|s_i - o_i|}{(s_i + o_i)/2}, \tag{A3}$$

$$\text{MFB} = \frac{1}{n}\sum_{i=1}^{n}\frac{s_i - o_i}{(s_i + o_i)/2}, \tag{A4}$$

where $\bar{o} = \frac{1}{n}\sum_{i=1}^{n} o_i$ and $\bar{s} = \frac{1}{n}\sum_{i=1}^{n} s_i$.

Appendix B Update formula for DA (PM$_{2.5}$ and PM$_{2.5-10}$)

In order to separately analyse PM$_{2.5}$ and PM$_{2.5-10}$ in the assimilation of lidar observations, the matrix $\mathbf{B}$ is modelled as follows

$$\mathbf{B} = \mathbf{PDP}^{\mathrm{T}}, \tag{B1}$$

where $\mathbf{D}$ is the error covariance matrix for PM$_{2.5}$ and PM$_{2.5-10}$. The matrix $\mathbf{D}$ is defined by

$$\mathbf{D} = \begin{bmatrix} \mathbf{D_{2.5}} & \mathbf{0} \\ \mathbf{0} & \mathbf{D_{2.5-10}} \end{bmatrix},$$

and the matrix $\mathbf{P}$ is defined by

$$\mathbf{P} = \begin{bmatrix} \mathbf{P_{2.5}} \\ \mathbf{P_{2.5-10}} \end{bmatrix},$$

where each column k of $\mathbf{P_{2.5}}$ (resp. $\mathbf{P_{2.5-10}}$) corresponds to the proportion of the mass of particles for a given species in a given size section in PM$_{2.5}$ (resp. PM$_{2.5-10}$) mass concentrations at grid point k as section 6.2 shown.

The matrix $\mathbf{Z}$ is defined by

$$\mathbf{Z} = \begin{bmatrix} \mathbf{Z_{2.5}} \\ \mathbf{Z_{2.5-10}} \end{bmatrix},$$

where the matrix $\mathbf{Z_{2.5}}$ (resp. $\mathbf{Z_{2.5-10}}$) is a $M \times (M \cdot N_b \cdot N_s)$ matrix, which converts the state vector $\mathbf{x}$ into the PM$_{2.5}$ (resp. PM$_{2.5-10}$) state $\mathbf{c_{2.5}}$ (resp. $\mathbf{c_{2.5-10}}$).

Let $\mathbf{S}' = \mathbf{SP}$. After multiplying each side of equation (18) by the matrix $\mathbf{Z}$, we obtain

$$\begin{pmatrix} \mathbf{c}^{\mathbf{a}}_{2.5} - \mathbf{c}^{\mathbf{b}}_{2.5} \\ \mathbf{c}^{\mathbf{a}}_{2.5-10} - \mathbf{c}^{\mathbf{b}}_{2.5-10} \end{pmatrix} = \mathbf{D}(\mathbf{LS}')^{\mathrm{T}}\left((\mathbf{LS}')\mathbf{D}(\mathbf{LS}')^t + \mathbf{R}\right)^{-1}\left(\mathbf{y} - H(\mathbf{x}^b)\right).$$

18

References

Balgovind, R., Dalcher, A., Ghil, M., and Kalnay, E.: A Stochastic-Dynamic Model for the Spatial Structure of Forecast Error Statistics, Mon.Weather Rev., 111, 701–722, 1983.

590 Bouttier, F. and Courtier, P.: Data assimilation concepts and methods, Meteorological Training Course Lecture Series, March 1999, ECMWF, 2002.

Boylan, J. W. and Russell, A. G.: PM and light extinction model performance metrics, goals, and criteria for three-dimensional air quality models, Atmos. Environ., 40, 4946–4959, 2006.

Brandt, J., Christensen, J. H., Frohn, L. M., Geels, C., Hansen, K. M., Hedegaard, G. B., Hvidberg, M.,

595 and Skjøth, C. A.: THOR – an operational and integrated model system for air pollution forecasting and management from regional to local scale, in: Proceedings of the 2nd ACCENT Symposium, 2007.

Chazette, P., Sanak, J., and Dulac, F.: New Approach for Aerosol Profiling with a Lidar Onboard an Ultralight Aircraft: Application to the African Monsoon Multidisciplinary Analysis, Environ. Sci. Technol., 41, 8335–8341, 2007.

600 Chazette, P., Bocquet, M., Royer, P., Winiarek, V., Raut, J.-c., Labazuy, P., Gouhier, M., Lardier, M., and Cariou, J.-p.: Eyjafjallajökull ash concentrations derived from both lidar and modeling, J. Geophys. Res., 117, 1–17, doi:10.1029/2011JD015755, 2012.

Collis, R. T. H. and Russell, P. B.: Lidar measurements of particles and gases by elastic backscattering and differential absorption, Top. Appl. Phys., 14(8), 8997, 1976.

605 Couvidat, F., Debry, E., Sartelet, K., and Seigneur, C.: A hydrophilic/hydrophobic organic (H2O) aerosol model: Development, evaluation and sensitivity analysis, J. Geophys. Res., 117, 1–19, doi:10.1029/2011JD017214, 2012.

Couvidat, F., Kim, Y., Sartelet, K., Seigneur, C., Marchand, N., Sciare, J., and Environnement, L. C.: Modeling secondary organic aerosol in an urban area: application to Paris, France, Atmos. Chem. Phys., 13, 983–996,

610 doi:10.5194/acp-13-983-2013, 2013.

DasGupta, M. and Mishra, S. K.: Least Absolute Deviation Estimation of Linear Econometric Models : A Literature Review, North-Eastern Hill University, 2007.

de Rooij, W. A. and van der Stap, C. C. A. H.: Expansion of Mie scattering matrices in generalized spherical functions, Astron. Astrophys., 131, 237248, 1984.

615 Debry, E., Fahey, K., Sartelet, K., Sportisse, B., , and Tombette, M.: Technical Note: A new SIze REsolved Aerosol Model (SIREAM), Atmos. Chem. Phys., 7, 1537–1547, doi:10.5194/acp-7-1537-2007, 2007.

Denby, B., Schaap, M., Segers, A., Builtjes, P., and Hora, J.: Comparison of two data assimilation methods for assessing PM$_{10}$ exceedances on the European scale, Atmospheric Environment, 42, 7122–7134, doi: 10.1016/j.atmosenv.2008.05.058, 2008.

620 Dockery, D. and Pope, A.: Epidemiology of acute health effects: summary of time-series, in: Particles in Our Air: Concentration and Health Effects, Harvard University Press, pp. 123–147, 1996.

Hess, M., Koepke, P., and Schult, I.: Optical Properties of Aerosols and Clouds: The Software Package OPAC, Bull. Amer. Meteor. Soc., 79, 831–844, 1998.

Hodzic, A., Chepfer, H., Vautard, R., Chazette, P., Beekmann, M., Bessagnet, B., Chatenet, B., Cuesta, J.,

625 Drobinski, P., Goloub, P., Haeffelin, M., and Morille, Y.: Comparison of aerosol chemistry transport model simulations with lidar and Sun photometer observations at a site near Paris, J. Geophys. Res., 109, 1–19,

doi:10.1029/2004JD004735, 2004.

Hodzic, A., Vautard, R., Chazette, P., Menut, L., and Bessagnet, B.: Aerosol chemical and optical properties over the Paris area within ESQUIF project, Atmos. Chem. Phys., 6, 3257–3280, doi:10.5194/acp-6-3257-2006, 2006.

Holben, B. N., Eck, T. F., Slutsker, I., Tanré, D., Buis, J. P., Setzer, A., Vermote, E., Reagan, J. A., Kaufman, Y. J., Nakajima, T., Lavenu, F., Jankowiak, I., and Smirnov, A.: AERONET - A federated instrument network and data archive for aerosol characterization, Remote. Sens. Environ., 66, 1–16, 1998.

Holben, B. N., Tanré, D., Smirnov, A., Eck, T. F., Slutsker, I., Abuhassan, N., Newcomb, W. W., Schafer, J. S., Chatenet, B., Lavenu, F., Kaufman, Y. J., Castle, J. V., Setzer, A., Markham, B., Clark, D., Frouin, R., Halthore, R., Karneli, A., Neill, N. T. O., Pietras, C., Pinker, R. T., Voss, K., and Zibordi, G.: An emerging ground-based aerosol climatology: Aerosol optical depth from AERONET, J. Geophys. Res., 106, 12 067–12 097, 2001.

Hong, S. Y., Noh, Y., and Dudhia, J.: A New Vertical Diffusion Package with an Explicit Treatment of Entrainment Processes, Mon.Weather Rev., 134, 2318–2341, 2006.

Intergoverment Panel on Climate Control (IPCC): Climate Change 2007, the fourth Assessment Report of the IPCC, Cambridge Univ. Press, 2007.

Jacobson, M. Z.: A physically-based treatment of elemental carbon optics: Implications for global direct forcing of aerosols, Geophys. Res. Lett., 27, 217–220, 2000.

Katrinak, K. A., Rez, P., Perkes, P. R., and Buseck, P. R.: Fractal geometry of carbonaceous agregates from an urban aerosol, Environ. Sci. Technol., 27, 539–547, 1993.

Kelly, J. T., Avise, J., Cai, C., and Kaduwela, A. P.: Simulating particle size distributions over California and impact on Lung deposition fraction, Aerosol Sci. Technol., 45, 148–162, doi:10.1080/02786826.2010.528078, 2011.

Kim, Y.: Air quality modeling: Evaluation of chemical and meteorological parameterizations, Ph.D. thesis, Université Paris-Est, 2011.

Kim, Y., Couvidat, F., Sartelet, K., and Seigneur, C.: Comparison of different gas-phase mechanisms and aerosol modules for simulating particulate matter formation, J. Air Waste Manage. Assoc., 61, 1218–1226, doi:10.1080/104732.89.2011.603939, http://dx.doi.org/10.1080/104732.89.2011.603939, 2011.

Kim, Y., Sartelet, K., Raut, J.-C., and Chazette, P.: Evaluation of the Weather Research and Forecast/urban model over Greater Paris, Boundary Layer Meteor., 149, 105–132, doi:10.1007/s10546-013-9838-6, 2013.

Kinne, S., Schulz, M., Textor, C., Guibert, S., Balkanski, Y., Bauer, S. E., Berntsen, T., Berglen, T. F., Boucher, O., Chin, M., Collins, W., Dentener, F., Diehl, T., Easter, R., Feichter, J., Fillmore, D., Ghan, S., Ginoux, P., Gong, S., Grini, A., Hendricks, J., Herzog, M., Horowitz, L., Isaksen, I., Iversen, T., Kloster, S., Koch, D., Kristjansson, J. E., Krol, M., Lauer, A., Lamarque, J. F., Lesins, G., Liu, X., Lohmann, U., Montanaro, V., Myhre, G., Penner, J. E., Pitari, G., Reddy, S., Seland, O., Stier, P., Takemura, T., Tie, X., Centre, H., Office, M., Unit, C. C., Sciences, G. E., Northwest, P., Fluid, G., and Arbor, A.: An AeroCom initial assessment - optical properties in aerosol component modules of global models, Atmos. Chem. Phys., 6, 1815–1834, doi:10.5194/acp-6-1815-2006, 2006.

Konovalov, I. B., Beekmann, M., Meleux, F., Dutot, A., and Foret, G.: Combining deterministic and statistical approaches for PM_{10} forecasting in Europe, Atmospheric Environment, 43, 6425–6434, doi:

10.1016/j.atmosenv.2009.06.039, http://dx.doi.org/10.1016/j.atmosenv.2009.06.039, 2009.

Lauwerys, R., Haufroid, V., Hoet, P., and Lison, D.: Toxicologie industrielle et intoxications professionnelles, Elsevier-Masson, 2007.

670 Li, Z., Zang, Z., Li, Q. B., Chao, Y., Chen, D., Ye, Z., Liu, Y., and Liou, K. N.: A three-dimensional variational data assimilation system for multiple aerosol species with WRF/Chem and an application to PM$_{2.5}$ prediction, Atmos. Chem. Phys., 13, 4265–4278, doi:10.5194/acp-13-4265-2013, 2013.

Mallet, V., Quélo, D., Sportisse, B., Ahmed de Biasi, M., Debry, E., Korsakissok, I., Wu, L., Roustan, Y., Sportisse, B., Sartelet, K., Tombette, M., and Foudhil, H.: Technical Note: The air quality modeling system
675 Polyphemus, Atmos. Chem. Phys., 7, 5479–5487, doi:10.5194/acp-7-5479-2007, 2007.

Ménard, R., Cohn, S. E., Chang, L.-P., and Lyster, P. M.: Assimilation of stratospheric chemical tracer observations using a Kalman filter. Part I: Formulation, Mon. Weather Rev., 128, 2654–2671, 1999.

Mishchenko, M. I., Travis, L. D., and Lacis, A. A.: Scattering, Absorption, and Emission of Light by Small Particles, Cambridge University Press, 2002.

680 Nenes, A., Pandis, S., and Pilinis, C.: ISORROPIA: A new thermodynamic equilibrium model for multiphase multi-component inorganic aerosols, Aquat. Geoch., 4, 123–152, 1998a.

Nenes, A., Pilinis, C., and Pandis, S. N.: Continued Development and Testing of a New Thermodynamic Aerosol Module for Urban and Regional Air Quality Models, Atmos. Env., 33, 1553–1560, 1998b.

Nicolet, M.: On the molecular scattering in the terrestrial atmosphere, Planet. Space Sci., 32, 14671468, doi:
685 10.1016/0032-0633(84)90089-8, 1984.

Pagowski, M. and Grell, G. A.: Experiments with the assimilation of fine aerosols using an ensemble Kalman filter, J. Geophys. Res., 117, 1–15, doi:10.1029/2012JD018333, 2012.

Pagowski, M., Grell, G. A., Mckeen, S. A., Peckham, S. E., and Devenyi, D.: Three-dimensional variational data assimilation of ozone and fine particulate matter observations: some results using the Weather Research
690 and Forecasting Chemistry model and Grid-point Statistical Interpolation, Q. J. R. Meteorol. Soc., 136, 2013–2024, doi:10.1002/qj.700, 2010.

Péré, J. C., Mallet, M., Pont, V., and Bessagnet, B.: Evaluation of an aerosol optical scheme in the chemistry-transport model CHIMERE, Atmospheric Environment, 44, 3688–3699, doi:10.1016/j.atmosenv.2010.06.034, http://dx.doi.org/10.1016/j.atmosenv.2010.06.034, 2010.

695 Randriamiarisoa, H., Chazette, P., Couvert, P., and Sanak, J.: Relative humidity impact on aerosol parameters in a Paris suburban area, Atmos. Chem. Phys., 6, 1389–1407, doi:10.5194/acp-6-1389-2006, 2006.

Raut, J.-C., Chazette, P., and Fortain, A.: New approach using lidar measurements to characterize spatiotemporal aerosol mass distribution in an underground railway station in Paris, Atmospheric Environment, 43, 575–583, doi:10.1016/j.atmosenv.2008.10.002, http://dx.doi.org/10.1016/j.atmosenv.2008.10.002, 2009a.

700 Raut, J.-C., Chazette, P., and Fortain, A.: Link between aerosol optical, microphysical and chemical measurements in an underground railway station in Paris, Atmospheric Environment, 43, 860–868, doi:10.1016/j.atmosenv.2008.10.038, http://dx.doi.org/10.1016/j.atmosenv.2008.10.038, 2009b.

Robinson, R. A. and Stokes, R. H.: Electrolyte solutions, Dover Publications, United Kingdom, 2002.

Royer, P., Chazette, P., Sartelet, K., Zhang, Q. J., and Beekmann, M.: Comparison of lidar-derived PM$_{10}$ with
705 regional modeling and ground-based observations in the frame of MEGAPOLI experiment, Atmos. Chem. Phys., 11, 10705–10726, doi:10.5194/acp-11-10705-2011, 2011.

Sachdeva, K. and Attri, A. K.: Morphological characterization of carbonaceous aggregates in soot and free fall aerosol samples, Atmospheric Environment, 42, 1025–1034, 2007.

Sartelet, K. N., Debry, E., Fahey, K. M., Roustan, Y., Tombette, M., and Sportisse, B.: Simulation of aerosols

710   and gas-phase species over Europe with the Polyphemus system. Part I: model-to-data comparison for 2001, Atmos. Environ., 29, 6116–6131, 2007.

Sartelet, K. N., Couvidat, F., Seigneur, C., and Roustan, Y.: Impact of biogenic emissions on air quality over Europe and North America, Atmospheric Environment, 53, 131–141, doi:10.1016/j.atmosenv.2011.10.046, http://dx.doi.org/10.1016/j.atmosenv.2011.10.046, 2012.

715 Schaap, M., Spindler, G., Schulz, M., Acker, K., Maenhaut, W., Berner, A., Wieprecht, W., Streit, N., Müller, K., Brüggemann, E., Chi, X., Putaud, J. P., Hitzenberger, R., Puxbaum, H., Baltensperger, U., and ten Brink, H.: Artefacts in the sampling of nitrate studied in the "INTERCOMP" campaigns of EUROTRAC-AEROSOL, Atmos. Environ., 48, 6487–6496, 2004.

Seinfeld, J. H. and Pandis, S. N.: Atmospheric chemistry and physics, Wiley-Interscience, 1998.

720 Simpson, D., Fagerli, H., Jonson, J. E., Tsyro, S., Wind, P., and Tuovinen, J. P.: Transboundary acidification, euthrophication and ground level ozone in Europe. Part I: unified EMEP model description, Technical Report, EMEP, 2003.

Skamarock, W. C., Klemp, J. B., Dudhia, J., Gill, D. O., Barker, D. M., Duda, M., Huang, X. Y., Wang, W., and Powers, J. G.: A Description of the Advanced Research WRF Version 3, NCAR Technical Note,

725   http://www.mmm.ucar.edu/wrf/users/docs/arw_v3.pdf, 2008.

Stromatas, S., Turquety, S., Menut, L., Chepfer, H., Pépé, J. C., Cesana, G., and Bessagnet, B.: Lidar signal simulation for the evaluation of aerosols in chemistry-transport models, Geosci. Model Dev., 5, 1543–1564, doi:10.5194/gmd-5-1543-2012, 2012.

Tombette, M., Chazette, P., Sportisse, B., and Roustan, Y.: Simulation of aerosol optical properties over Europe

730   with a 3-D size-resolved aerosol model: comparisons with AERONET data, Atmos. Chem. Phys., 8, 7115–7132, doi:10.5194/acp-8-7115-2008, 2008.

Tombette, M., Mallet, V., and Sportisse, B.: PM_{10} data assimilation over Europe with the optimal interpolation method, Atmos. Chem. Phys., 9, 57–70, doi:10.5194/acp-9-57-2009, 2009.

Wang, K. C., Dickinson, R. E., and Liang, S. L.: Clear sky visibility has decreased over land globally from

735   1973 to 2007, Science, 323, 1468–1470, 2009.

Wang, Y., Sartelet, K. N., Bocquet, M., and Chazette, P.: Assimilation of ground versus lidar observations for PM_{10} forecasting, Atmos. Chem. Phys., 13, 269–283, doi:10.5194/acp-13-269-2013, 2013.

Winker, D. M., Hunt, W. H., Mcgill, M. J., Lidar, C.-a., and Satellite, I. P.: Initial performance assessment of CALIOP, Geophysical Research Letters, 34, 1–5, doi:10.1029/2007GL030135, 2007.

740 Wu, L., Mallet, V., Bocquet, M., and Sportisse, B.: A comparison study of data assimilation algorithms for ozone forecasts, J. Geo. Res., 113, 1–17, doi:10.1029/2008JD009991, 2008.

Yarwood, G., Rao, S., Yocke, M., and Whitten, G.: Updates to the Carbon Bond Chemical Mechanism: CB05 Final Report to the US EPA, RT-0400675, http://www.camx.com/publ/pdfs/CB05_Final_Report_120805.pdf, 2005.

745 Zhang, Y., Sartelet, K., Zhu, S., Wang, W., Wu, S.-Y., Zhang, X., Wang, K., Tran, P., Seigneur, C., and Wang, Z.-F.: Application of WRF/Chem-MADRID and WRF/Polyphemus in Europe Part 2: Evaluation of chem-

22

Table 1. Dry CRI and density for different aerosol species at $\lambda = 355$ nm. Re (resp. Im) stands for the real (resp. imaginary) part of CRI.

Species	Re	Im	density (g cm^{-3})
Nitrate	1.53	-0.005	1.5
Ammonium	1.53	-0.005	0.91
Black carbon	1.75	-0.4645	2.25
Mineral dust	1.53	-0.0166	2.33
Organics	1.53	-0.008	1.3
Sulfate	1.45	-1e-08	1.84
Sodium	1.509	-2.946e-07	0.97
Chlorate	1.509	-2.946e-07	1.15
Water	1.35738	2.72875e-08	1.0

Table 2. Statistics (see Appendix A) of the simulation results for the Airparif network during the MEGAPOLI summer experiment. Obs. stands for observation. Sim. stands for simulation. Corr. stands for correlation.

Day	PM$_{10}$						PM$_{2.5}$					
	Obs. mean μg m^{-3}	Sim. mean μg m^{-3}	RMSE μg m^{-3}	Corr. %	MFB %	MFE %	Obs. mean μg m^{-3}	Sim. mean μg m^{-3}	RMSE μg m^{-3}	Corr. %	MFB %	MFE %
All	21.53	14.14	10.79	64	-42	49	12.59	12.78	6.02	68	4	39
01 July	44.99	29.39	18.08	78	-45	47	28.82	27.14	7.94	74	-10	23
04 July	18.37	11.11	8.34	8	-48	48	10.80	9.99	3.90	-25	-4	31
16 July	26.25	16.47	12.28	16	-41	46	12.60	15.76	5.41	31	25	34
21 July	27.84	16.84	13.13	28	-46	50	15.46	16.19	5.84	14	6	31
26 July	18.04	10.12	9.52	-4.6	-52	53	12.32	10.27	5.05	7.1	-16	34
29 July	29.25	12.33	18.49	28	-76	78	14.82	11.78	7.32	38	-20	37

ical concentrations, sensitivity simulations, and aerosol-meteorology interactions, Atmos. Chem. Phys., 13, 6845–6875, doi:10.5194/acp-13-6845-2013, 2013.
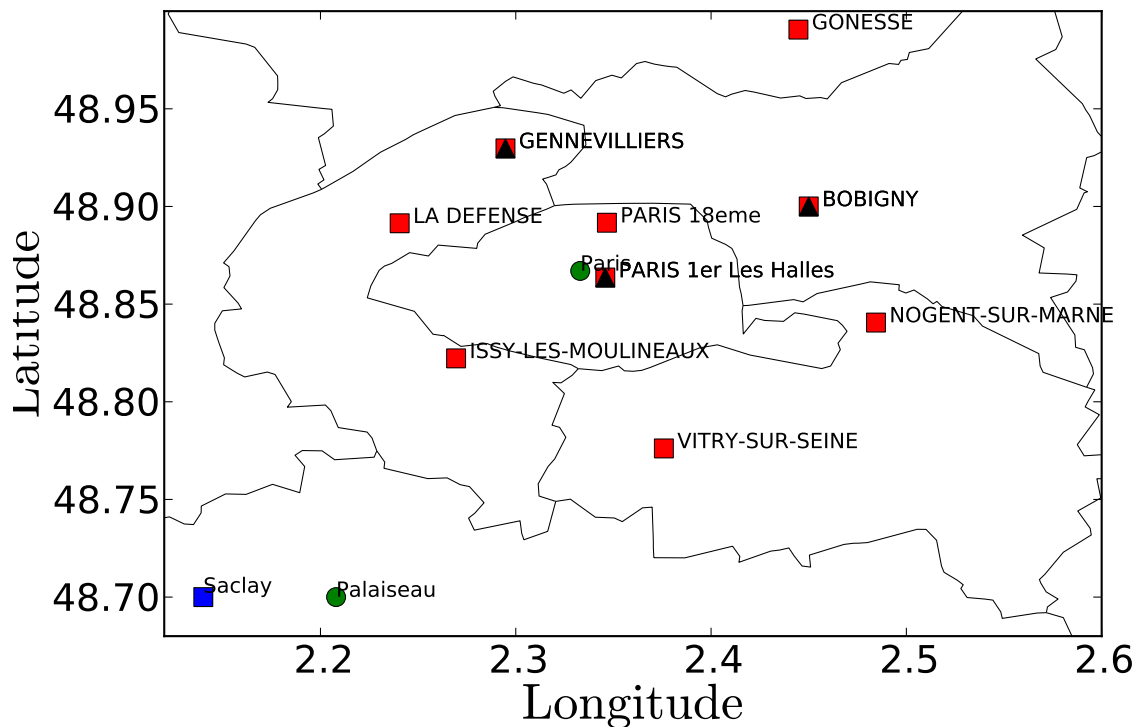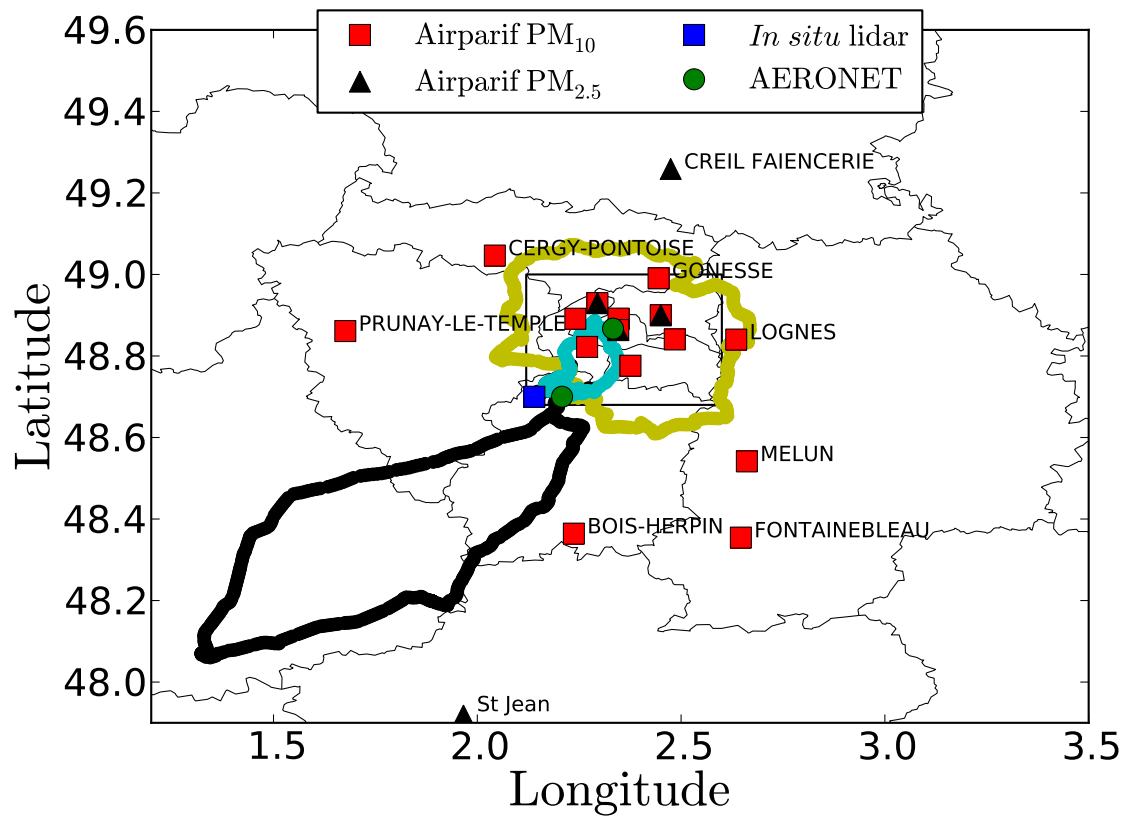
Fig. 1. The blue square shows the location of the ground-based *in situ* lidar station, the red squares (resp. the black triangles) show the locations of Airparif stations for PM$_{10}$ (resp. PM$_{2.5}$) measurements and the green discs show the locations of AERONET stations. The black pattern shows the GBML track on 01 July 2009. The yellow and cyan patterns show two GBML tracks on 26 July 2009. The rectangle area is detailed in the bottom figure.
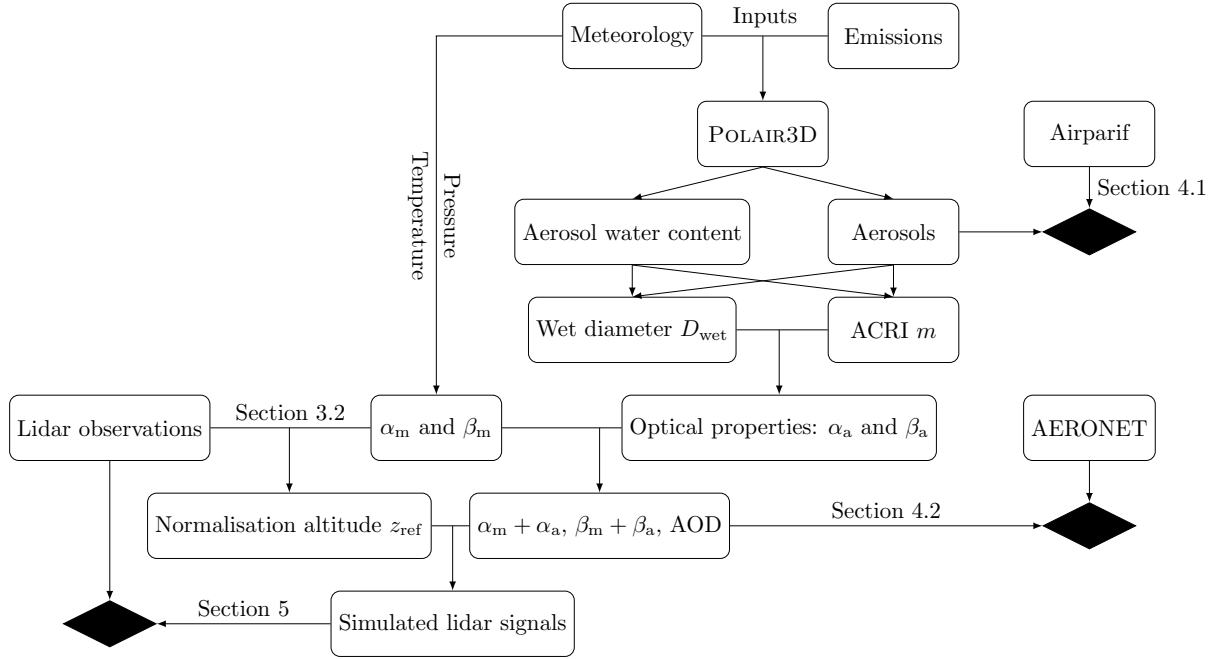
Fig. 2. Diagram describing the methodology for lidar signals modelling from outputs of the air-quality model POLAIR3D. Comparisons to measurements are performed at black nodes. ACRI stands for aerosol complex refractive index. β_m (resp. β_a) is the molecular (resp. aerosol) backscatter coefficient. α_m (resp. α_a) is the molecular (resp. aerosol) extinction coefficient.

Table 3. Statistics (see Appendix A) of the simulation results for the AERONET network for different lidar measurement days.

Day	Obs. mean	Sim. mean	RMSE	MFB %	MFE %
01 July	0.59	0.47	0.20	-21	29
04 July	0.25	0.14	0.12	-58	58
16 July	0.26	0.18	0.08	-33	33
26 July	0.15	0.08	0.07	-53	53
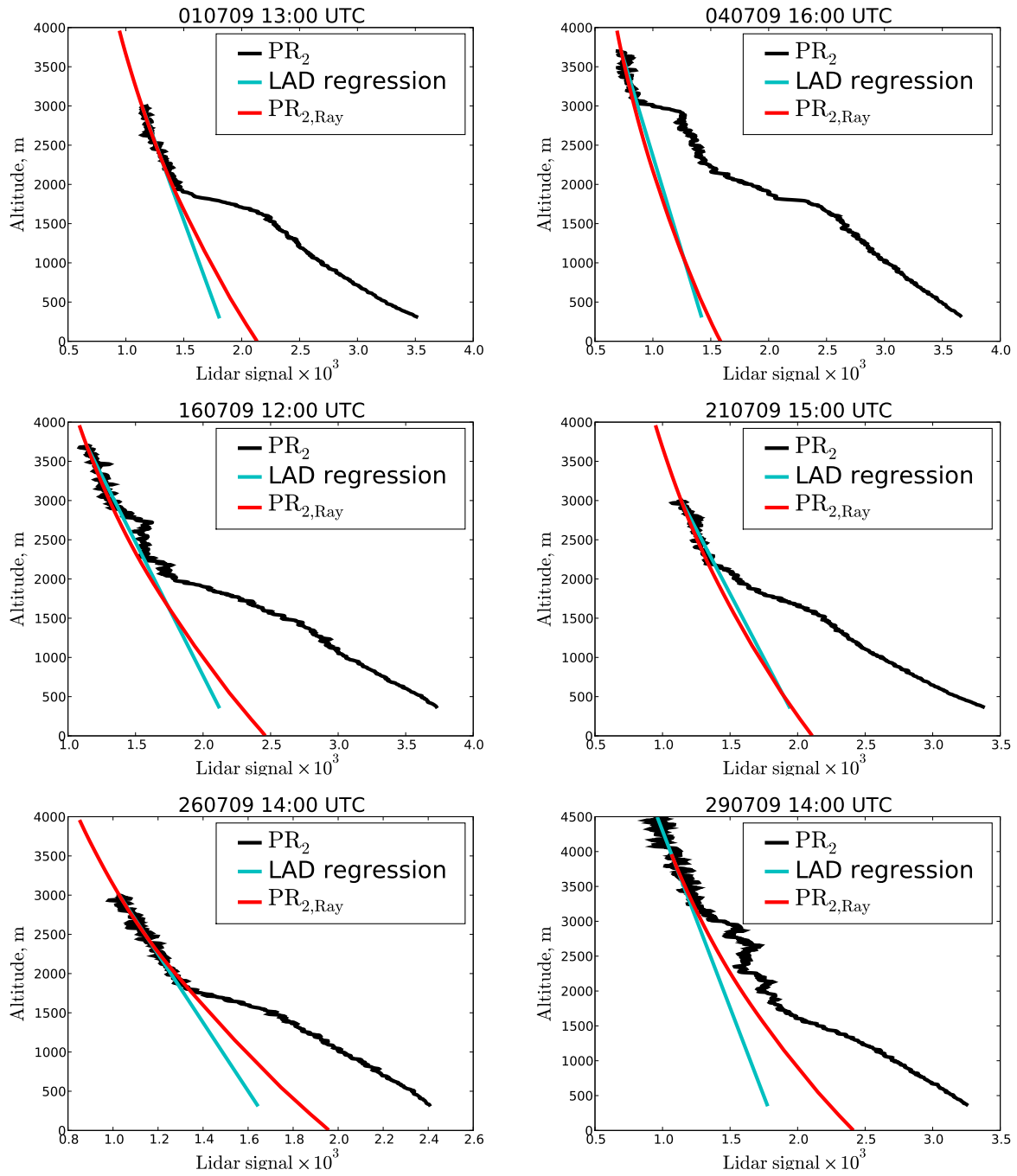
Fig. 3. Black lines (resp. red lines) indicate lidar signals PR_2 (resp. simulated molecular signals $PR_{2,Ray}$) at 13:00 UTC 01, 16:00 UTC 04, 12:00 UTC 16, 15:00 UTC 21, 14:00 UTC 26 and 14:00 UTC 29 July 2009 (blue points). LAD regressions of weighted lidar measurement points are indicated by cyan lines.
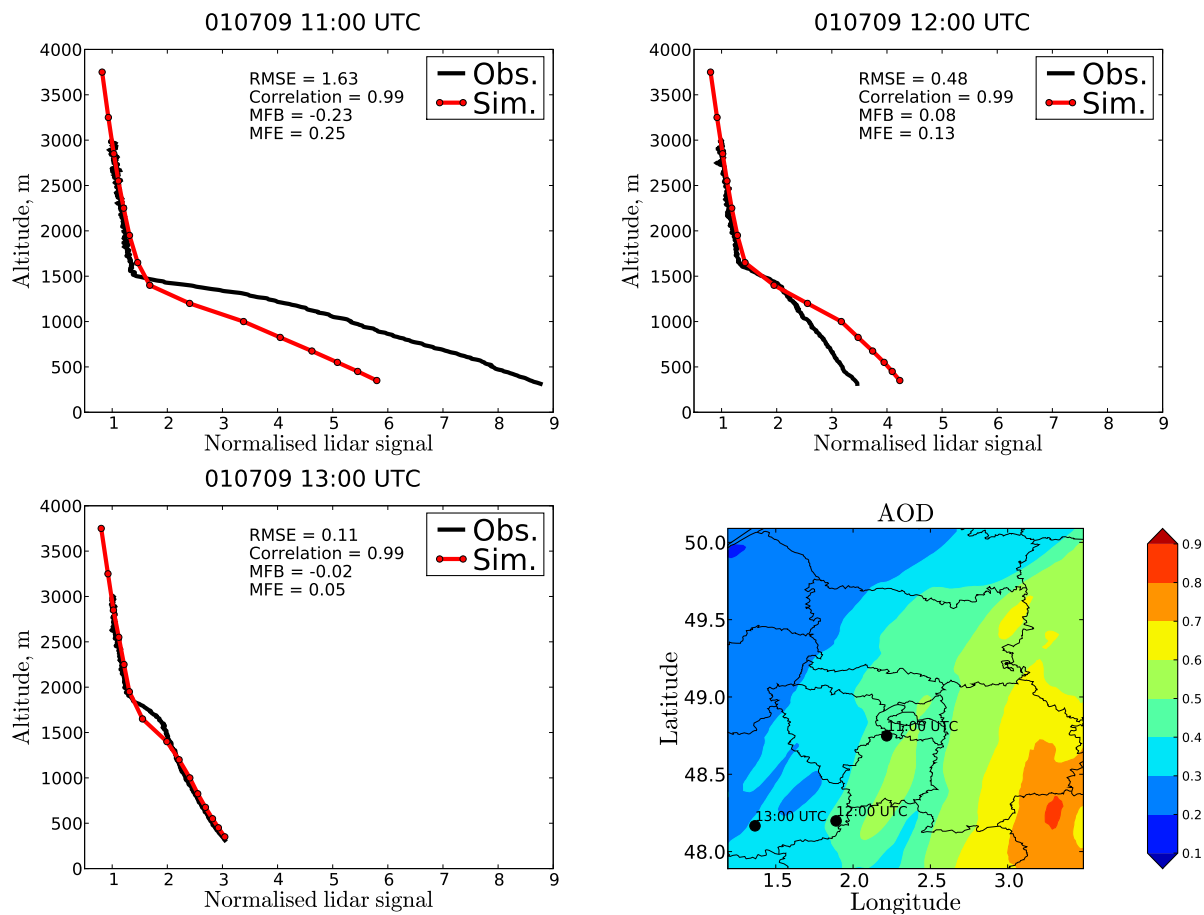
Fig. 4. Comparisons between the vertical profiles observed by GBML (black lines) and simulated by POLYPHE-MUS (red lines) on 01 July 2009 at 11:00, 12:00 and 13:00 UTC. Lidar observations below the altitude of full overlap are not represented. The lower right panel shows the positions of the different lidar profiles and the horizontal distribution of the mean of the AODs at 11:00, 12:00 and 13:00 UTC.
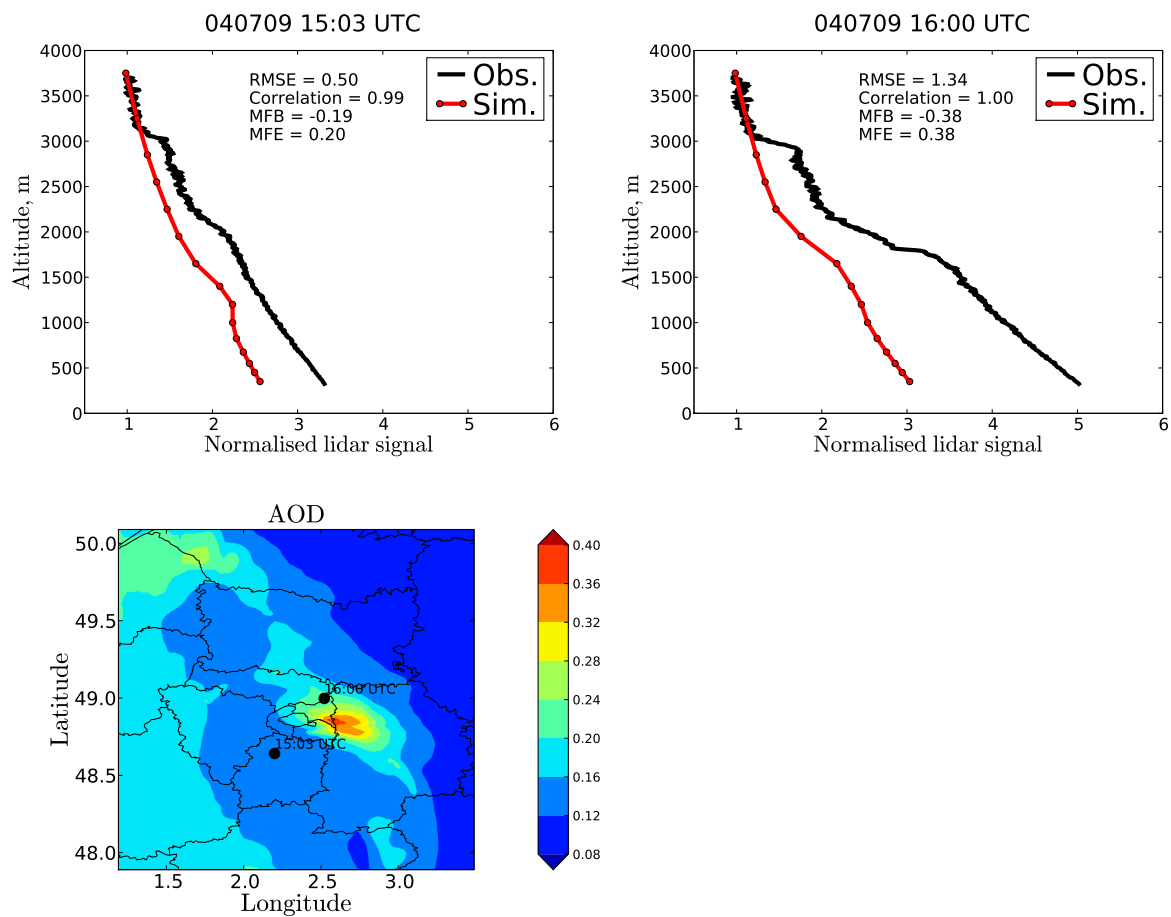
Fig. 5. Comparisons between the vertical profiles observed by GBML (black lines) and simulated by Polyphe-
mus (red lines) on 04 July 2009 at 15:03 and 16:00 UTC. Lidar observations below the altitude of full overlap
are not represented. The lower left panel shows the positions of the different lidar profiles and the horizontal
distribution of the mean of the AODs at 15:00 and 16:00 UTC.
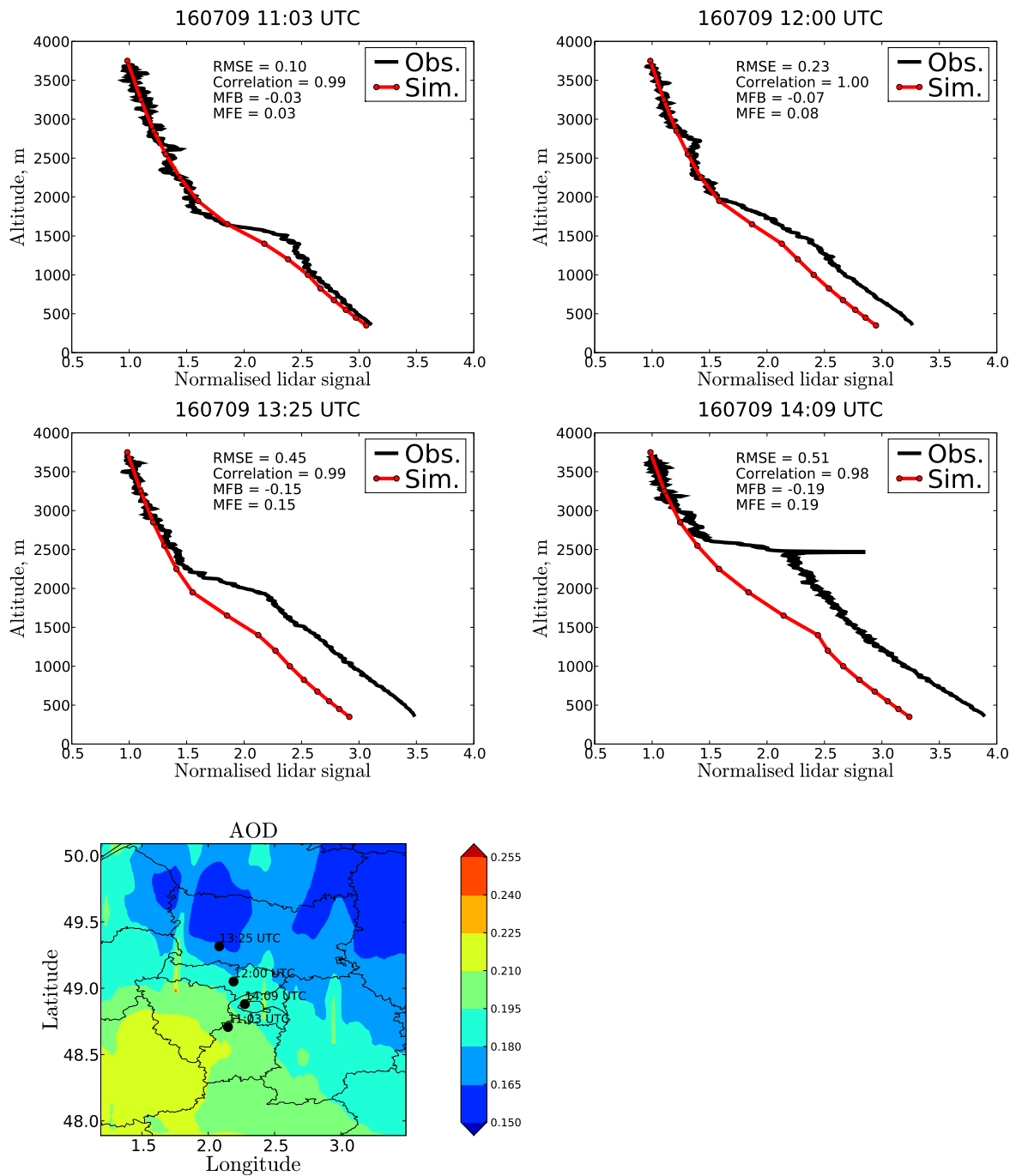
Fig. 6. Comparisons between the vertical profiles observed by GBML (black lines) and simulated by POLYPHE-MUS (red lines) on 16 July 2009 at 11:03, 12:00, 13:25 and 14:09 UTC. Lidar observations below the altitude of full overlap are not represented. The lower left panel shows the positions of the different lidar profiles and the horizontal distribution of the mean of the AODs at 11:00, 12:00, 13:00 and 14:00 UTC.
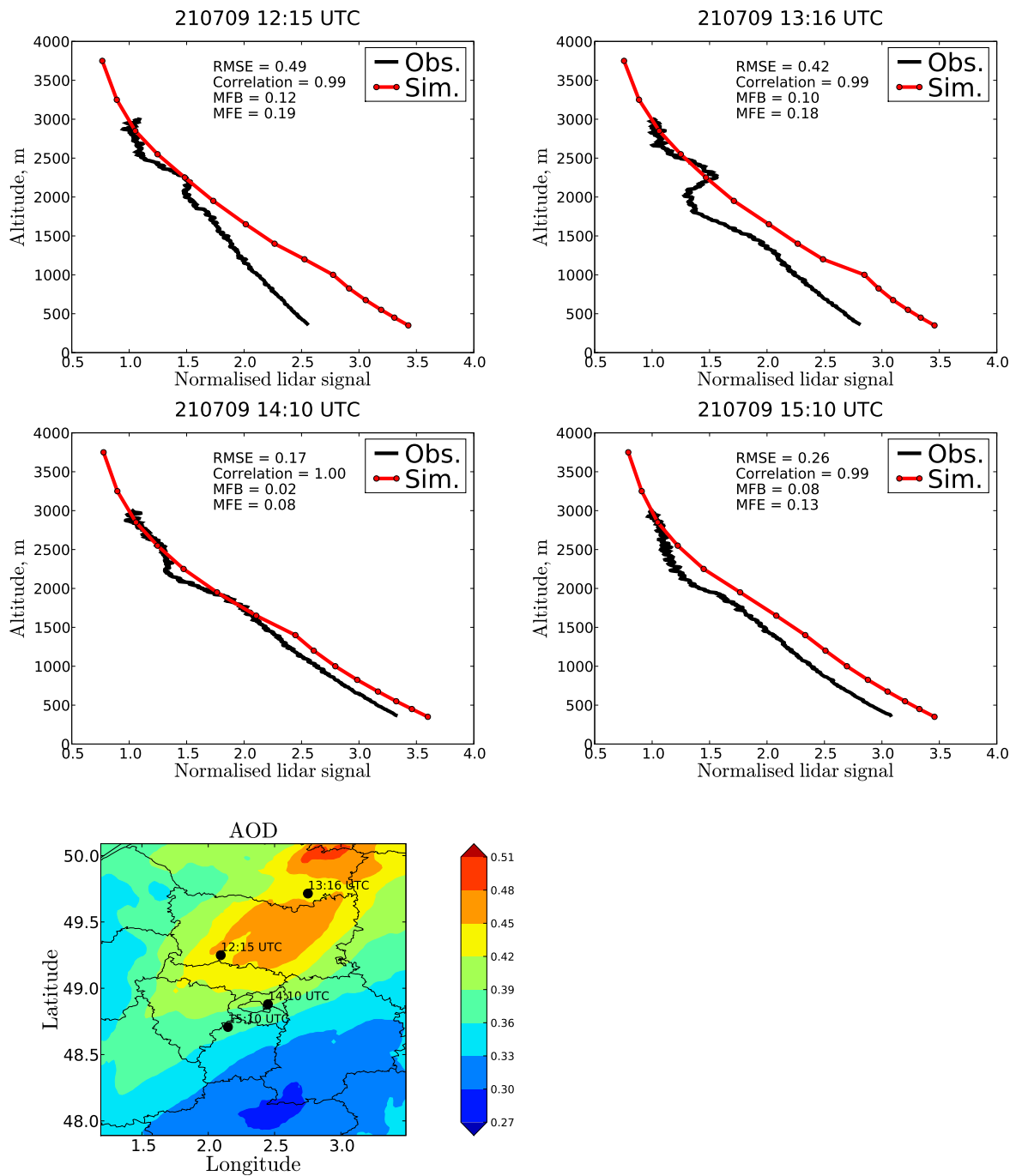
Fig. 7. Comparisons between the vertical profiles observed by GBML (black lines) and simulated by POLYPHE-MUS (red lines) on 21 July 2009 at 12:15, 13:16, 14:10 and 15:10 UTC. Lidar observations below the altitude of full overlap are not represented. The lower left panel shows the positions of the different lidar profiles and the horizontal distribution of the mean of the AODs at 12:00, 13:00, 14:00 and 15:00 UTC.
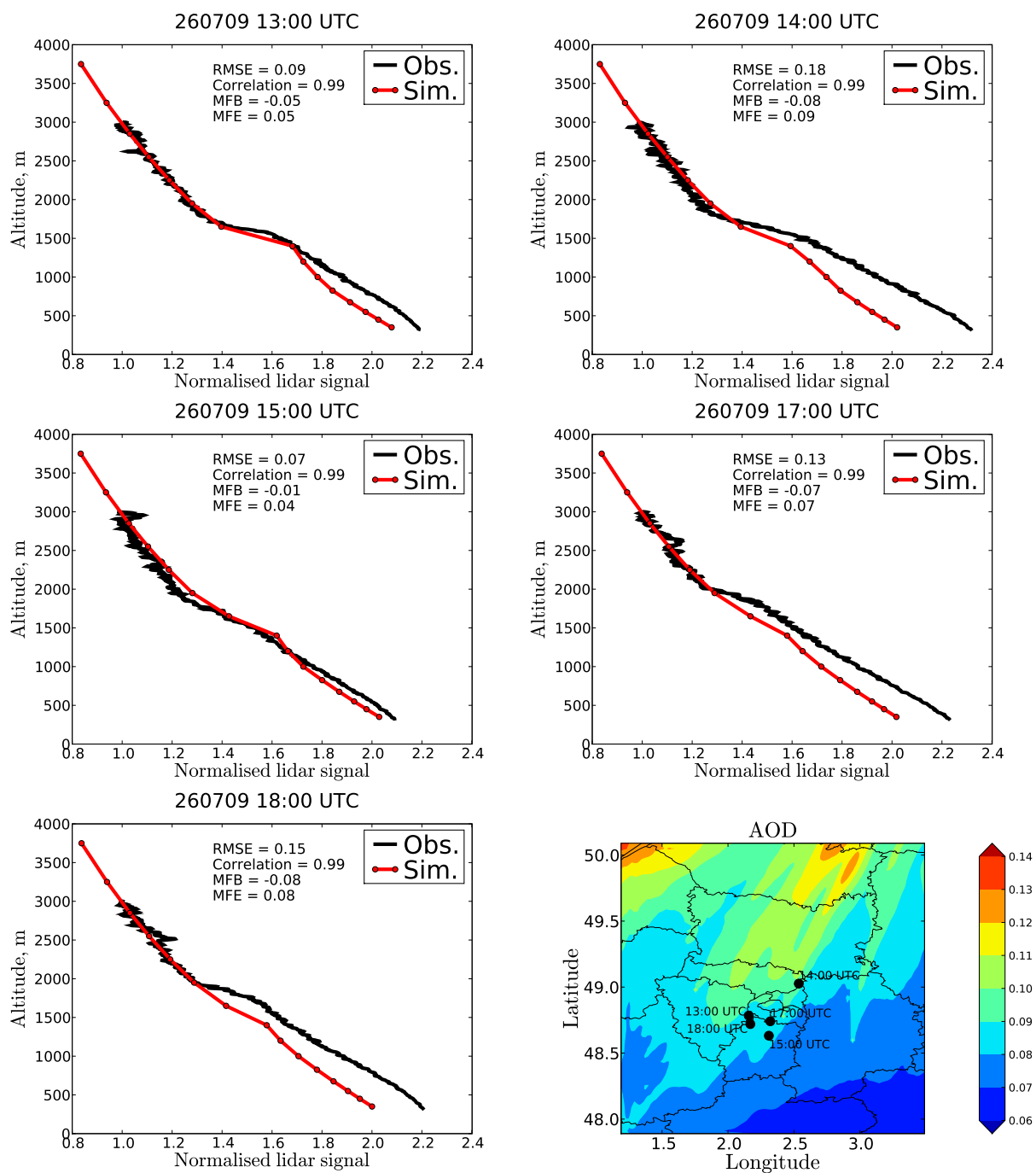
Fig. 8. Comparisons between the vertical profiles observed by GBML (black lines) and simulated by POLYPHE-MUS (red lines) on 26 July 2009 at 13:00, 14:00, 15:00, 17:00 and 18:00 UTC. Lidar observations below the altitude of full overlap are not represented. The lower right panel shows the positions of the different lidar profiles and the horizontal distribution of the mean of the AODs at 13:00, 14:00, 15:00, 17:00 and 18:00 UTC.

31
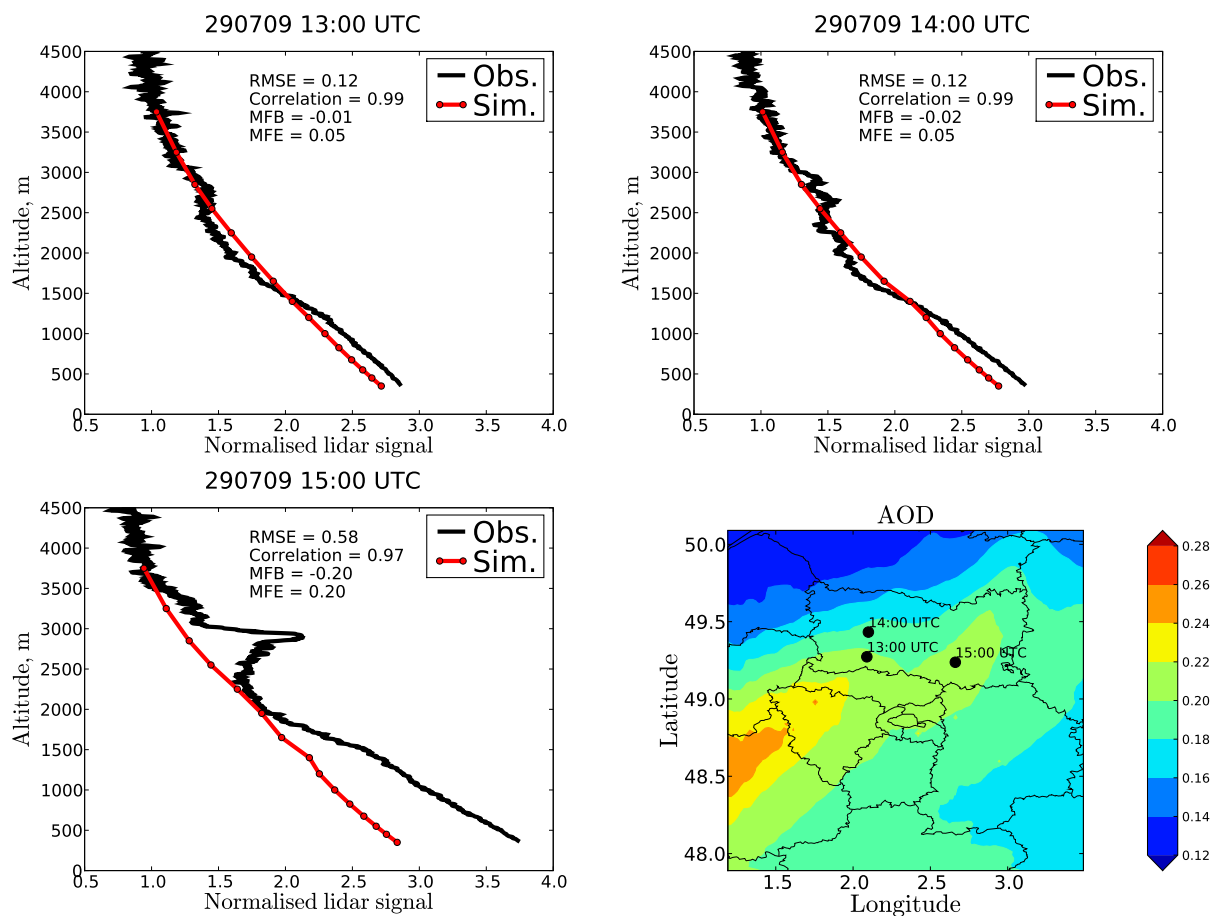
Fig. 9. Comparisons between the vertical profiles observed by GBML (black lines) and simulated by POLYPHE-MUS (red lines) on 29 July 2009 at 13:00, 14:00 and 15:00 UTC. Lidar observations below the altitude of full overlap are not represented. The lower right panel shows the positions of the different lidar profiles and the horizontal distribution of the mean of the AODs at 13:00, 14:00 and 15:00 UTC.
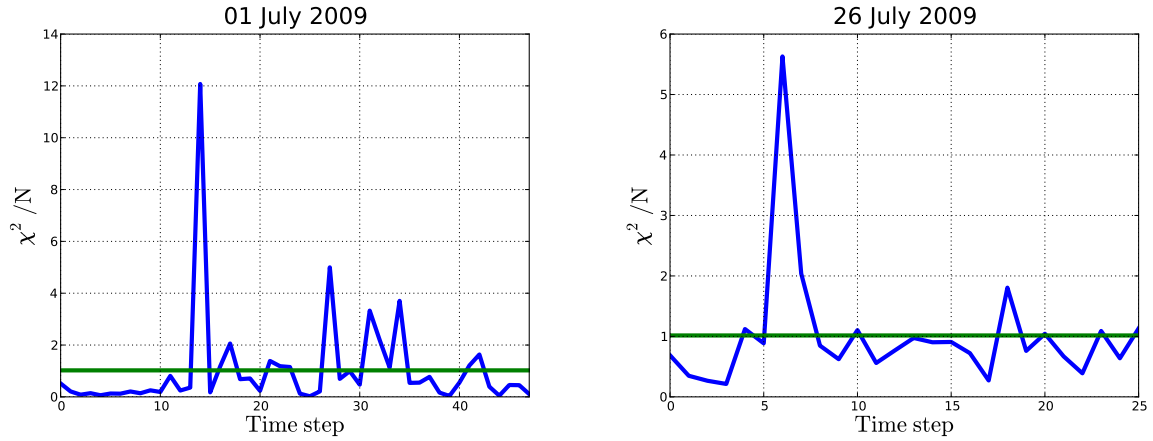
Fig. 10. Time evolution of χ^2/N (blue lines) for DA runs on 01 and 26 July 2009. The mean over DA window of χ^2/N is 1.02 (resp. 1.02) for 01 (resp. 26) July 2009.

Table 4. Statistics (see Appendix A) of the simulation results (PM_{10} and $PM_{2.5}$) without DA and with DA for the Airparif network for 01 and 26 July 2009. "With DA (PM_{10})" stands for the assimilation of lidar observations correcting directly PM_{10}. "With DA ($PM_{2.5}$ and $PM_{2.5-10}$)" stands for the assimilation of lidar observations correcting separately $PM_{2.5}$ and $PM_{2.5-10}$.

Day	Species	Simulation	Stations	Obs. mean $\mu g\, m^{-3}$	Sim. mean $\mu g\, m^{-3}$	RMSE $\mu g\, m^{-3}$	Corr. %	MFB %	MFE %
01 July	PM_{10}	Without DA	15	47.26	32.35	17.74	84	-41	43
		With DA (PM_{10})			36.20	13.69	90	-29	32
		With DA ($PM_{2.5}$ and $PM_{2.5-10}$)			39.85	11.63	84	-19	25
	$PM_{2.5}$	Without DA	5	30.52	30.21	8.54	69	-5	23
		With DA (PM_{10})			33.04	10.44	59	5	27
		With DA ($PM_{2.5}$ and $PM_{2.5-10}$)			33.08	10.45	58	5	27
26 July	PM_{10}	Without DA	15	16.25	9.96	6.67	-20	-47	47
		With DA (PM_{10})			10.55	6.08	15	-42	42
		With DA ($PM_{2.5}$ and $PM_{2.5-10}$)			12.80	4.73	26	-25	30
	$PM_{2.5}$	Without DA	5	10.25	8.99	2.80	7	-9	25
		With DA (PM_{10})			9.64	2.51	22	-2	22
		With DA ($PM_{2.5}$ and $PM_{2.5-10}$)			9.49	2.54	21	-4	22
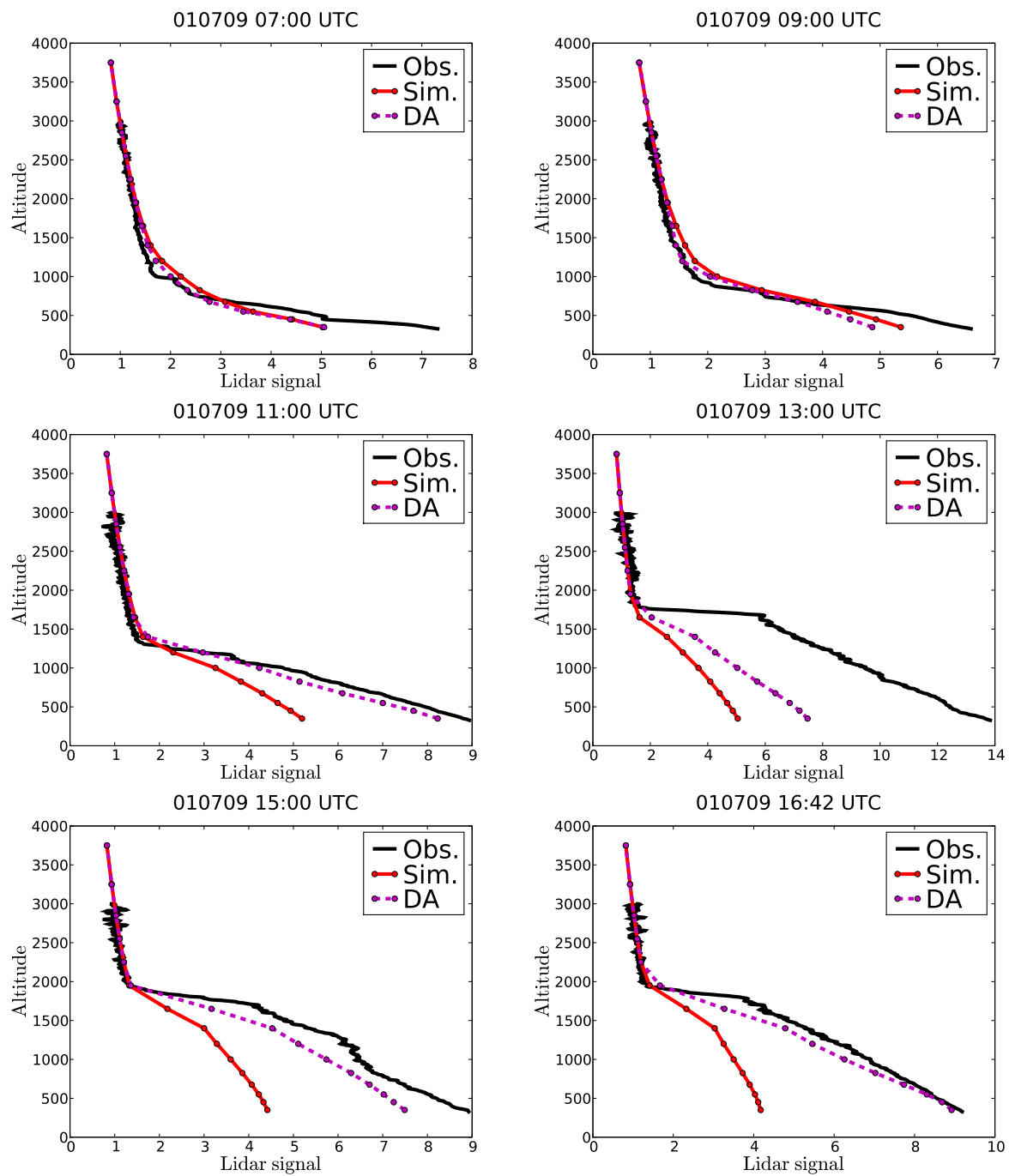
Fig. 11. Lidar vertical profiles observed by the ground-based *in situ* lidar at Saclay (black lines), simulated without DA (red lines) and simulated with DA (magenta lines) on 01 July 2009.